Numerical Heat Transfer, Part A: Applications
An International Journal of Computation and Methodology

ISSN: 1040-7782 (Print) 1521-0634 (Online) Journal homepage: www.tandfonline.com/journals/unht20

Optimizing energy generation in power-law nanofluid flow through curved arteries with gold nanoparticles

Bhupendra K. Sharma, Chandan Kumawat & Muhammad Mubashir Bhatti

NUMERICAL HEAT TRANSFER, PART A: APPLICATIONS
2024, VOL. 85, NO. 18, 3058–3090
https://doi.org/10.1080/10407782.2023.2232123

Optimizing energy generation in power-law nanofluid flow through curved arteries with gold nanoparticles

Bhupendra K. Sharma[a], Chandan Kumawat[a], and Muhammad Mubashir Bhatti[b,c]

[a]Department of Mathematics, Birla Institute of Technology and Science, Pilani, India; [b]College of Mathematics and Systems Science, Shandong University of Science and Technology, Qingdao, P.R. China; [c]Material Science, Innovation and Modelling (MaSIM) Research Focus Area, North-West University, Mmabatho, South Africa

ABSTRACT

The investigation of blood flow into curved arteries is fascinating and essential to prevent the advancement of vascular disease. Motivated by electro-kinetic manipulation, gold nanoparticles, and their size applications, a mathematical model is developed to explain blood flow, entropy generation, and electro-kinetic energy conversion (EKEC) efficiency in curved arterial flow. To make this study more realistic, a patient-specific overlapped stenosis condition and non-Newtonian (power-law fluid) blood flow model have been considered. The effects of a magnetic field, external heating, and chemical reactions are also included. The Stone's strongly implicit scheme has been considered to solve the system of non-linear partial differential equations (PDE's) in the" MATLAB" software. In this numerical investigation, an error tolerance of 10^{-6} has been considered for every iteration step under Stone's scheme. The significance of various physical parameters, such as nanoparticle volume fraction (m), their size (dp), magnetic field intensity (M), inverse Debye length ($\bar{\kappa}$), flow behavior index (Sc), heat source (H), and chemical reaction parameter (ξ) on the blood flow velocity, temperature, concentration, EKEC efficiency, and entropy generation have been explained graphically. This study also developed stream function contours to describe flow trapping patterns. The findings of this study conclude that the blood flow EKEC efficiency reduces with the presence of nanoparticles and stenosis in the artery. In addition, both flow velocity and entropy enhance by adopting large-size nanoparticles instead of small diametric nanoparticles. Clinical researchers and biologists may use the results of this computational study to forecast endothelial cell damage and plaque deposition in curved arteries with WSS profiles, by which the severity of these conditions can be reduced.

ARTICLE HISTORY
Received 20 March 2023
Revised 25 May 2023
Accepted 26 June 2023

KEYWORDS
Blood flow; EKEC efficiency; entropy generation; gold nanoparticle; power-law fluid

1. Introduction

The study of microfluidics in micro-electromechanical systems (MEMS) is a fascinating topic because of its important applications in both physical and biological processes. The presence of salt and minerals, such as sodium, potassium, magnesium, chloride, etc., in the blood, makes it an electrolyte solution. Therefore, when blood (electrolyte) in come touch with the arterial wall, it forms a thin electric double layer (EDL) at the wall. The study of electrokinetic force on the flow, which has Power-law fluid properties, has been performed by Chakraborty et al. [1,2]. In this study, they analyzed blood flow velocity for the different hematocrit levels and electric field

CONTACT Muhammad Mubashir Bhatti mmbhatti@sdust.edu.cn; mubashirme@yahoo.com College of Mathematics and Systems Science, Shandong University of Science and Technology, Qingdao 266590, P.R. China.

Nomenclature

$\bar{r}, \bar{\Theta}, \bar{z}$	dimensional form of radial, angular, and axial directions, respectively	B	uniform magnetic field in dimensional form
$\tilde{r}, \tilde{\Theta}, \tilde{z}$	non-dimensional form of radial, angular, and axial directions, respectively	$\vec{J}$	electric current density
		$\bar{P}$	dimensional pressure
R_0	radius of healthy artery	Q	heat Source
a	location of stenosis	R_c	dimensional form of chemical reaction parameter
Ψ	total electric potential		
$\tilde{\psi}_i, \tilde{\psi}_a$	dimensional form of induced and streaming electric potential, respectively.	$\bar{\chi}$	electro-kinetic energy conversion efficiency
ρ_{el}, Ξ	net electric charge density and dielectric constant, respectively.	M	magnetic field parameter
		Pr	Prandtl number
dp, db	nanoparticle and blood diameter, respectively	Br	Brinkman number
		Ec	Eckert number
m	nanoparticle volume fraction	ε	arterial curvature parameter
$\bar{U}, \bar{V}, \bar{W}$	dimensional velocity of in $\bar{r}, \bar{\Theta}, \bar{z}$ directions, respectively	WSS	wall shear stress
		Q	flow rate
$\bar{T}, \bar{C}$	dimensional temperature and concentration profiles, respectively	λ	frictional impedance
		Nu	Nusselt number

strength. A theoretical study to describe the effect of EDL thickness and flow behavior index on the flow through a slit microchannel has been proposed by Zhao et al. [3]. The numerical discussion of high zeta potential effects on the flow through a curved microchannel by adopting the SIMPLE algorithm to solve momentum equations has been performed by Nekoubin [4]. This study considers power-law fluid properties and states that the axial velocity and flow rate enhances with a positive add-in zeta potential. Recently, an analytical study using the perturbation technique to discuss electrokinetic flow and energy conversion in curved tubes has been published by Ding et al. [5]. This study concluded that electrokinetic energy conversion efficiency is higher in curved tubes in comparison with straight tubes. Also, EDL potential is higher at the outer side bend of a curved tube than at the inner side. Recently, a computational study to analyze heat transfer phenomena for electro-osmotic driven flow under the peristaltic action for curved and straight tubes has been given by Nooren et al. [6,7].

The study of streaming potential and electrokinetics energy conversion (EKEC) is a very fascinating topic for researchers when fluid flows in microchannels. The conversion process of mechanical energy produced by pressure-driven flow and chemical energy of EDL into electric energy is called EKEC. Badopadhyaay et al. [8], performed a numerical investigation to determine the energy transfer efficiency in the narrow channel for power-law fluid and stated that mechanical energy conversion has been improved for the shear-thinning fluids in comparison with the Newtonian fluids with the no-slip boundary condition. The limitation of wall surface potential (zeta potential $\tilde{\phi}$) limit on the streaming potential and hydroelectric energy conversion efficiency for Phan-Thein-Tanner (PTT) fluid has been discussed by Sarkar [9]. They found that streaming potential and EKEC enhances for the $6 < \tilde{\phi} \leq 6$ and for $6 < \tilde{\phi} \leq 10$ they shows reverse effect. Jian et al. [10,11], discussed the EKEC efficiency in the cylindrical flow in the presence of nanoparticle and concluded that for a certain limit of Debye length, both EKEC efficiency and streaming potential decreases with the increment in nanoparticle volume fraction.

In the last few decades, discovering the application of nanotechnology has been a curious topic for researchers in the field of medicine, thermal engineering, industry, etc. Nano-particles are very small in size with a diameter range between 1 and 100 um and it enhances the thermal properties of the fluid. Wilczewska et al. [12] state that due to small dimension size, nanoparticles reflect their unique biological property to penetrate the tissue and cell membranes, which helps in the direct interaction of nanoparticles with the proteins and smaller cells. At present time there are so many nanoparticles with different nanostructures that have been used for diagnosing several diseases, such as Caelyx® (Liposomes nanostructure with doxorubicin to cure ovarian and breast cancer), Tricor® (Nanocrystalline drugs with Fenofibrate in Hypercholesterolemia treatment), Amphotec® (Lipid colloidal dispersion nanostructure with Amphotericin B in cure of Fungal infections), etc. [13]. Due to biocompatibility and magnetic properties, ultra superparamagnetic iron oxide (USPIO) nanoparticles are used in magnetic resonance imaging (MRI) and computed tomography (CT) to identify the situation of plaque deposition in arteries to prevent myocardial infarction [14]. Duivendvoorden et al. [15], performed an experimental study and explained that the use of a high dose of rHDL nanoparticle in statins therapy can reduce atherosclerosis deposition. Weinstein et al. [16] describe the importance of superparamagnetic iron oxide nanoparticles in the healing process of the nervous system and also obtained significantly good diagnosis results on the low tesla magnet. A computational study to describe the effect of different nanoparticles, such as Cu, TiO_2, and Al_2O_3 on the stenosed curved arterial blood flow under an external body acceleration situation has been conducted by Zaman et al. [17]. Sultan et al. [18] developed a mathematical to study both time-dependent diseased sections stenosis and aneurysm for a curved arterial flow. In this study, they adopted the Nano-Erying-Powell fluid properties for the blood and solved the governing equations using the finite difference method. Recently, Poonam et al. [19] adopted the Crank-Nicolson method to computationally investigate the effect of (Au-Al_2O_3/blood) hybrid-nanofluid in a curved artery. This investigation considered both stenosis and aneurysm arterial conditions to make this study more realistic. They suggested that adding the quantity of Al_2O_3 nanoparticles into Au-blood nanofluid helps boost the flow temperature, which may be beneficial during thermal therapies to kill cancer and tumor cells.

In the last few decades, the study of the magnetic field effect in biological fluids has attracted the attention of researchers as the human body experience different intensities of the magnetic field in their day-to-day life. The presence of a high concentration quantity of hemoglobin in RBC, intercellular protein, and cell membrane allows the blood flow to function like a bio-magnetic fluid. There are numerous applications of the magnetic field that can be seen in the medical field, such as using magnetic devices for cell separation [20], lowering the bleeding during surgery and cancer therapy [21], nanomagnetic particles in targeting drug delivery [22], and magnetic tracer development, etc. [23]. Firstly, Issacci et al. [24], numerically discussed the induced magnetic field concept in the curved pipe by considering a toroidal coordinate system. They found the solution in the power series form for both low and intermediate Hartmaan numbers and explained that with enhancing magnetic field intensity, the fluid compression improves near the tube wall in velocity contours. To demonstrate the effect of induced magnetic voltage on arterial and tissue blood flow, a numerical study is investigated by Kinouchi et al. [25]. They stated that magnetic-induced voltage in the aorta can produce electric signals in the heart and its surrounding tissues whenever an arterial wall is supposed to be non-electric in mathematical models. This study also describes that, after a significant limit of magnetic field intensity (10 T), the reduction in blood flow rate becomes significantly small. Mekheimer et al. [26] conducted an analytical study of an induced magnetic field using a catheter in a tapered overlapped stenosed artery and the results show that axial magnetic field induction enhances the increase in magnetic field strength and exhibits the reverse nature with magnetic Reynold number. A numerical observation to distinguish the impact of cilia length and the Hall effect on the flow through cylindrical tubes has been discussed by Farooq et al. [27], and they state that with the increase in cilia length, flow produces more entropy. Recently, Sharma et al. [28] performed a numerical study to understand the effect of magnetic field on the two-phase blood flow through curved stenosed artery for the toroidal coordinate system and revealed that the risk of lipid deposition increases with the rise in curvature and magnetic field strength.

All the cited research articles in the literature survey provide information about fluid behavior phenomena and heat transport for fluid flow in curved and straight tubes. As per the author's best knowledge, the power-law fluid model for blood flow with electric potential (for EDL potential) and the EKEC concept have not been studied earlier. Therefore, the prime objective of this article is to investigate the fluid phenomena (velocity, temperature, concentration, wall shear stress, Nusselt number), entropy generation, and EKEC efficiency for the blood flow (power-law fluid) through an overlapped stenosed curved artery. In the mathematical modeling, the effects of gold nanoparticles and their size have also been considered to describe their impact on blood flow. In curved tubes, it is very difficult to compute the analytical solution of a system of non-linear partial differential equations (Navier-Stokes and Poission-Boltzmann). Therefore, in this research work, a second-order finite difference scheme [29] has been adopted to discretize these systems of non-linear PDE's, after which these equations are solved using Stone's strongly implicit method [30] by considering the tolerance of 10^{-6}. The results for fluid physical phenomenas, such as velocity, temperature, concentration, EKEC, entropy generation, WSS, and Nusselt number have been computed numerically by using "MATLAB" software and explained using graphs.

The novelty of present investigation includes:

- The effect of gold nanoparticles on the non-Newtonian blood flow (power-law fluid) through overlapped stenosed curved artery has been examined.
- The effect of nanoparticle size on the physical fluid phenomena has been investigated.
- The electric potential and EKEC efficiency profile for blood flow has been obtained.
- The entropy generation profile for blood flow for various physical parameters has been figure out.

2. Problem formulation

In this study, investigation of laminar, incompressible blood flow through an overlapped stenosed curved artery has been performed. In this study, blood is considered a non-Newtonian fluid; therefore, properties of the power-law fluid have been taken into account for governing equation formation. In this investigation, blood flows through the curved artery, and the toroidal coordinate system $(\bar{r}, \bar{\Theta}, \bar{z})$ have been employed to describe the arterial geometry. The z-axis represents the curved artery axis, r is taken along the radial direction and $\bar{\Theta}$ represent the angular direction. Figures 1 and 2 differentiate the real healthy and stenosed curved artery.

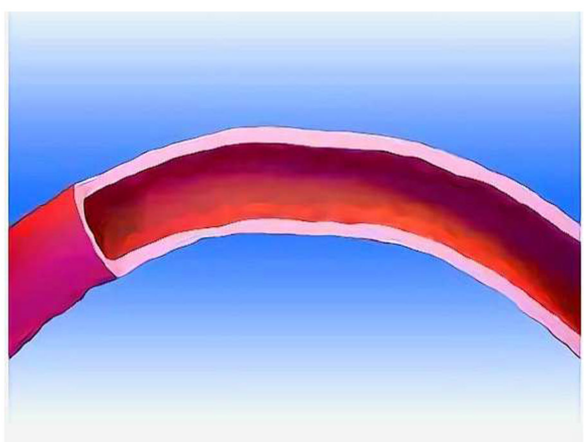

Figure 1. Healthy curved artery.

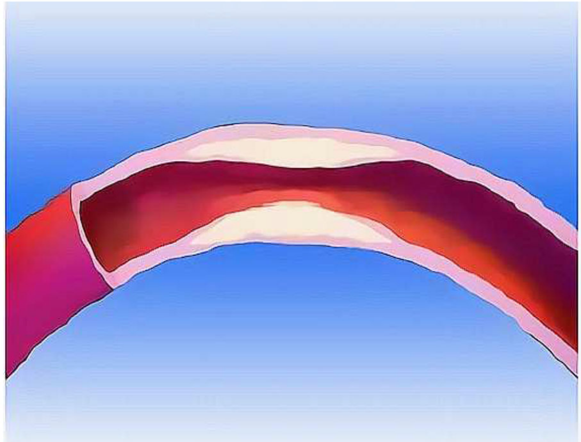

Figure 2. Stenosed curved artery.

2.1. Mathematical formulation of stenosis

The computational study of cardiovascular diseases is essential and risk-free to predict the current state and severity of the disease compared to experimental studies. In the computational study, the effects of different flow conditions can be studied, which is impossible in the experimental study. Generally, most of the arterial geometry is curved instead of straight. Therefore, in this study, blood flow phenomena have been discussed for curved arterial flow. An overlapped arterial diseases section has been considered to make this mathematical study more accurate with the realistic stenosed arterial flow. This idea has come from the Ahmed et al. [31] published work. In this work, they studied blood phenomena in overlapped stenosed curved artery under different circumstances. The time-dependent overlapped diseased artery section (stenosis) condition has been assumed for modeling of the curved arterial flow. $R(z, t)$ represent the artery radius in the stenotic region. The arterial wall has been considered negatively charged. Figure 3 presents the geometry of stenosed curved artery. Numerically formulation of diseases section (stenosis) written as preceding [31]:

Mathematical formulation of overlapped stenosis:

$$R(\bar{z},t) = \begin{cases} \left[R_0 - \dfrac{\Delta(\bar{z}-a)}{L_0}\left(11 - \dfrac{94}{3L_0}(\bar{z}-a) + \dfrac{32}{L_0^2}(\bar{z}-a)^2 - \dfrac{32}{3L_0^3}(\bar{z}-a)^3\right)\right]\varrho(t), & a \le \bar{z} \le a + \dfrac{3}{2}L_0 \\ R_0\varrho(t) \quad \text{Rest region.} \end{cases} \tag{1}$$

$$\varrho(t) = 1 - \kappa(\cos(\Omega t) - 1)e^{-\kappa\Omega t}. \tag{2}$$

where $\frac{3}{2}L_0$ and L represents the length of overlapped diseases section of artery, respectively. Δ and a indicates the stenosis maximum height and starting stenosis location, respectively.

κ is constant.

2.2. Electrostatic potential

The presence of salt and minerals, such as sodium, potassium, magnesium, chloride, etc., in the blood makes it an electrolyte solution. Therefore, when blood with a uniform dielectric constant (Ξ) flows into a curved artery, it induces inter-facial charges on the arterial wall. The induced charges allow the moving free ions into the blood to establish a thin electric double layer (EDL)

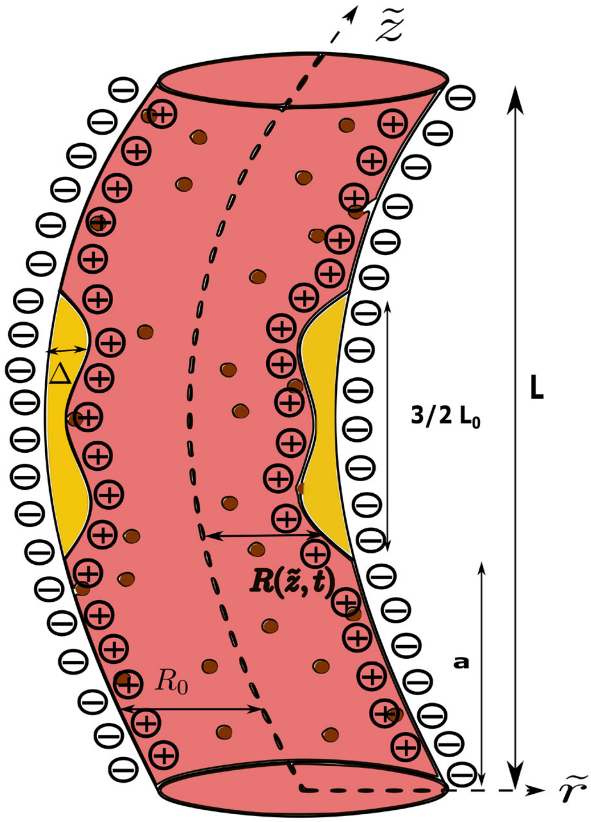

Figure 3. Graphical representation of curved artery.

at the arterial wall. In this EDL, an electric potential field ($\tilde{\psi}_i$) is generated with the net zero-charge density. Whereas a streaming(external) potential ($\tilde{\psi}_a$) occurs in the blood flow due to an externally applied electric field, which produces a net flow charge. The total electric potential (Ψ) is the combination of both induced (ψ_i) and streaming potential ($\tilde{\psi}_a$), i.e. $\Psi = \tilde{\psi}_i + \tilde{\psi}_a$. For a uniformly charged curved artery, electric potential can be written in the form of the Poisson equation

$$\nabla^2 \Psi = -\frac{\tilde{\rho}_{el}}{\Xi}, \tag{3}$$

where ρ_{el} represents the net electric charge density.

This study considered the flow through the curved artery; therefore, induced electric potential (ψ_i) also varies in the angular direction ($\bar{\Theta}$) along with the radial direction ($\bar{r}$), i.e. $\tilde{\psi}_i = \tilde{\psi}_i(\bar{r}, \bar{\Theta})$, and streaming potential have only axial dependence i.e. $\psi_a = \psi_a(\bar{z})$ [5,32]. By substituting these assumptions into Eq. (3), we get

$$\nabla^2 \tilde{\psi}_i(\bar{r}, \bar{\Theta}) = -\frac{\tilde{\rho}_{el}}{\Xi}, \tag{4}$$

$$\nabla^2 \tilde{\psi}_a(\bar{z}) = 0, \tag{5}$$

i.e.

$$\frac{\partial^2 \tilde{\psi}_a}{\partial \bar{z}^2} = 0$$

This indicates that $\frac{\partial \tilde{\psi}_a}{\partial \bar{z}}$ is constant, so it can be written as

$$\tilde{E}_s = -\frac{\partial \tilde{\psi}_a}{\partial \bar{z}} \tag{6}$$

The condition of symmetric electrolyte condition $(\Upsilon_+ = -\Upsilon_- = \Upsilon_v)$ has been considered, therefore the mathematical formulation of net electric charge density can be specified as

$$\tilde{\rho}_{el} = e(\Upsilon_+ n_+ + \Upsilon_- n_-) = e\Upsilon_v(n_- - n_-), \tag{7}$$

where e and Υ_v represent the electron charge and valence respectively, whereas n_+, n_- describe the cation and anion density quantity, respectively. The density of these charged ions can be determined using Boltzmann distribution

$$n_\pm = n_0 \exp\left(\mp \frac{\Upsilon_v e \tilde{\psi}_i}{K_B T_{la}}\right), \tag{8}$$

where n_0 denotes the ion density of the bulk fluid, K_B and T_{la} symbolize the Boltzmann constant and local absolute temperature.

With the substituting the mathematical expression of ρ_{el} and $n_\pm$ from Eqs. (7) and (8) into the Eq. (3), we get

$$\nabla^2 \tilde{\psi}_i = \kappa^2 \tilde{\psi}_i \tag{9}$$

where κ denotes the electro-kinetic width (Inverse of Debye length)

Debye length $\lambda = \sqrt{\frac{\Xi K_B T_{la}}{2 n_0 e^2 \Upsilon_v^2}}$

The applied body force on the blood flow through the curved artery is the combination of both electric and magnetic field force. Therefore, the mathematical expression of electromagnetic body force can be formulated as

$$\vec{F}_{em} = \tilde{\rho}_{el}\vec{E} + \vec{J} \times \vec{B} \tag{10}$$

The generalized Ohm's law is written as [33]

$$\begin{aligned} \vec{J} &= \sigma(\vec{E} + \vec{V} \times \vec{B}) \\ \vec{E} &= -\nabla\Psi \end{aligned} \tag{11}$$

where $\vec{E}, \vec{J},$ and $\vec{B}$ denotes the electric field, electric current density, and magnetic field, respectively. $\vec{V}$ indicates the flow velocity and $\vec{V} = (\bar{U}, \bar{V}, \bar{W})$ are the velocity components in the $\bar{r}, \bar{\Theta}, \bar{z}$ directions, respectively.

2.3. Nanoparticle

The injection of gold (Au) nanoparticles in the blood flow is beneficial in diagnosing several serious diseases. The nanoparticle volume fraction, as well as its particle size, also reflects the critical role in flow physiology. Therefore this study considers the particle size effect on the nanofluid viscosity and thermal conductivity.

The thermal conductivity and viscosity of the nanofluid using Corcione's model [34]

$$\frac{K^{nf}}{K^b} = 1 + 4.4 Re_p^{0.4} Pr^{0.66}\left(\frac{T_b}{T_{fr}}\right)^{10}\left(\frac{K^p}{K^b}\right)^{.03} m^{0.66} \tag{12}$$

$$\frac{\mu^{nf}}{\mu^b} = \frac{1}{1 - 34.87\left(\frac{dp}{db}\right)^{-0.3} m^{1.03}} \tag{13}$$

where,

$$Re_p = \frac{2\rho^b \bar{k}_b T_b}{\pi(\mu^b)^2 d_p},$$
$$d_f = 0.1\frac{6M_a}{N\pi\rho^b}$$

where, K^{nf} and μ^{nf} represent the thermal conductivity and viscosity of nanofluid (Au + blood), respectively.

K^b, μ^b, T_b, and db denote the blood thermal conductivity, viscosity, temperature, and blood cells diameter, respectively. m is the volume fraction of nanoparticle.

Re_p is the particle Reynolds number, T_{fr} blood freezing temperature, and dp is nanoparticle diameter.

$\bar{k}_b$ is Boltzmann constant (1.38064×10^{-23})

M_a is molecular weight of base fluid (Blood)

N is Avogadro number

The remaining thermal properties of nanofluid are considered according to Brinkman model are written as [35,36]

$$\begin{cases} \dfrac{\rho^{nf}}{\rho^b} = (1-m) + m\left(\dfrac{\rho^p}{\rho^b}\right) \\ \dfrac{\sigma^{nf}}{\sigma^b} = \dfrac{\sigma^p + (m-1)\sigma^b - (m-1)m(\sigma^b - \sigma^p)}{\sigma^p + (m-1)\sigma^b + m(\sigma^b - \sigma^p)} \\ \dfrac{Dp^{nf}}{Dp^b} = \dfrac{1-m}{1+m/2} \end{cases} \tag{14}$$

where, ρ^{nf}, σ^{nf}, and Dp^{nf} are the density, electrical conductivity, and mass diffusivity of nanofluid, respectively.

ρ^b, σ^b, Dp^b are the density, electrical conductivity, and mass diffusivity of blood, respectively, and ρ^p, σ^p are the density, electrical conductivity of nanoparticle (gold), respectively.

2.4. Governing equations

The Power-law fluid has been considered for the arterial blood flow and stress component for this fluid is written as follows [37]

$$(\tau)_{ij} = -\bar{P}I + K\mu^{nf}\Omega_f \ \phi_{ij}, \tag{15}$$

where

$$\Omega_f = \left[(\phi)^2_{\bar{r}\bar{r}} + (\phi)^2_{\bar{\Theta}\bar{\Theta}} + (\phi)^2_{\bar{z}\bar{z}} + 2((\phi)^2_{\bar{r}\bar{\Theta}} + (\phi)^2_{\bar{\Theta}\bar{z}} + (\phi)^2_{\bar{z}\bar{r}})\right]^{\frac{q-1}{2}}.$$

where, τ and ϕ represents the stress and strain tensors, respectively. K and q represent the flow consistency and flow behavior index, respectively. μ^{nf} state the nanofluid viscosity.

The governing equations for curved artery can be written as follows [38,39]

$$\frac{h}{D}\frac{\partial \bar{W}}{\partial \bar{z}} + \frac{\partial \bar{U}}{\partial \bar{r}} + \frac{1}{\bar{r}}\frac{\partial \bar{V}}{\partial \bar{\Theta}} + \frac{\bar{U}}{\bar{r}} + \frac{\bar{U}\cos\bar{\Theta} - \bar{V}\sin\bar{\Theta}}{D} = 0, \tag{16}$$

where, h denotes the radius of curvature.

$$D = h + \bar{r}\cos\bar{\Theta}$$

Momentum equations

$\bar{r}$-direction:

$$\rho^{nf}\left(\frac{\partial \bar{U}}{\partial t}+\frac{h\bar{W}}{D}\frac{\partial \bar{U}}{\partial \bar{z}}+\bar{U}\frac{\partial \bar{U}}{\partial \bar{r}}+\frac{\bar{V}}{\bar{r}}\frac{\partial \bar{U}}{\partial \bar{\Theta}}-\frac{\bar{V}^2}{\bar{r}}-\frac{\bar{W}_c^2\cos\bar{\Theta}}{D}\right)=\frac{h}{\bar{r}D}\Big(\frac{\partial}{\partial \bar{z}}(\bar{r}(\tau)_{\bar{r}\bar{z}})+\frac{\partial}{\partial \bar{r}}\left(\frac{D\bar{r}(\tau)_{\bar{r}\bar{r}}}{h}\right)$$
$$+\frac{\partial}{\partial \bar{\Theta}}\left(\frac{D(\tau)_{\bar{r}\bar{\Theta}}}{h}\right)\Big)-\frac{(\tau)_{\bar{\Theta}\bar{\Theta}}}{\bar{r}}-\frac{\cos\bar{\Theta}(\tau)_{\bar{z}\bar{z}}}{D}+\tilde{\rho}_{el}\vec{E}_{\bar{r}}+(\vec{J}\times\vec{B})_{\bar{r}}, \tag{17}$$

$\bar{\Theta}$ direction:

$$\rho^{nf}\left(\frac{\partial \bar{V}}{\partial t}+\frac{\bar{W}h}{D}\frac{\partial \bar{V}}{\partial \bar{z}}+\bar{U}\frac{\partial \bar{V}}{\partial \bar{r}}+\frac{\bar{V}}{\bar{r}}\frac{\partial \bar{V}}{\partial \bar{\Theta}}+\frac{\bar{U}\bar{V}}{\bar{r}}+\frac{\bar{W}^2\sin\bar{\Theta}}{D}\right)=\frac{h}{\bar{r}D}\Big(\frac{\partial}{\partial \bar{z}}(\bar{r}(\tau)_{\bar{\Theta}\bar{z}})+\frac{\partial}{\partial \bar{r}}\left(\frac{D\bar{r}(\tau)_{\bar{r}\bar{\Theta}}}{h}\right)$$
$$+\frac{\partial}{\partial \bar{\Theta}}\left(\frac{D(\tau)_{\bar{\Theta}\bar{\Theta}}}{h}\right)\Big)+\frac{(\tau)_{\bar{r}\bar{\Theta}}}{\bar{r}}+\frac{\sin\bar{\Theta}(\tau)_{\bar{z}\bar{z}}}{D}+\tilde{\rho}_{el}\vec{E}_{\bar{\Theta}}+(\vec{J}\times\vec{B})_{\bar{\Theta}}, \tag{18}$$

$\bar{z}$ direction:

$$\rho_c^{nf}\left(\frac{\partial \bar{W}}{\partial t}+\frac{\bar{U}\bar{W}\cos\bar{\Theta}}{D}+\frac{\bar{W}h}{D}\frac{\partial \bar{W}}{\partial \bar{z}}+\bar{U}\frac{\partial \bar{W}}{\partial \bar{r}}-\frac{\bar{V}\bar{W}\sin\bar{\Theta}}{D}+\frac{\bar{V}}{\bar{r}}\frac{\partial \bar{W}}{\partial \bar{\Theta}}\right)=\frac{h}{\bar{r}D}\left(\frac{\partial}{\partial \bar{z}}(\bar{r}(\tau)_{\bar{z}\bar{z}}\right)$$
$$+\frac{\partial}{\partial \bar{r}}\left(\frac{D\bar{r}(\tau)_{\bar{r}\bar{z}}}{h}\right)+\frac{\partial}{\partial \bar{\Theta}}\left(\frac{D(\tau)_{\bar{\Theta}\bar{z}}}{h}\right)\Big)+\frac{\cos\bar{\Theta}\;(\tau)_{\bar{r}\bar{z}}}{D}-\frac{\sin\bar{\Theta}(\tau)_{\bar{z}\bar{\Theta}}}{D}+\tilde{\rho}_{el}\vec{E}_{\bar{z}}+(\vec{J}\times\vec{B})_{\bar{z}}, \tag{19}$$

Energy equation:

$$\rho^{nf}\bar{C}_p^{nf}\left(\frac{\partial \bar{T}}{\partial t}+\bar{U}\frac{\partial \bar{T}}{\partial \bar{r}}+\frac{\bar{V}}{\bar{r}}\frac{\partial \bar{T}}{\partial \bar{\Theta}}+\frac{\bar{W}h}{D}\frac{\partial \bar{T}}{\partial \bar{z}}\right)=K^{nf}\left(\frac{\partial^2\bar{T}}{\partial \bar{r}^2}+\frac{1}{\bar{r}}\frac{\partial \bar{T}}{\partial \bar{r}}+\frac{h^2}{D^2}\frac{\partial^2\bar{T}}{\partial \bar{z}^2}+\frac{\cos\bar{\Theta}}{D}\frac{\partial \bar{T}}{\partial \bar{r}}-\frac{\sin\bar{\Theta}}{\bar{r}D}\frac{\partial \bar{T}}{\partial \bar{\Theta}}+\frac{1}{\bar{r}^2}\frac{\partial^2\bar{T}}{\partial \bar{\Theta}^2}\right)$$
$$+Q+\bar{I}+\frac{\vec{J}\cdot\vec{J}}{\sigma^{nf}}, \tag{20}$$

Concentration equation:

$$\left(\frac{\partial \bar{C}}{\partial t}+\bar{U}\frac{\partial \bar{C}}{\partial \bar{r}}+\frac{\bar{V}}{\bar{r}}\frac{\partial \bar{C}}{\partial \bar{\Theta}}+\frac{\bar{W}h}{D}\frac{\partial \bar{C}}{\partial \bar{z}}\right)=Dp^{nf}\left(\frac{\partial^2\bar{C}}{\partial \bar{r}^2}+\frac{1}{\bar{r}}\frac{\partial \bar{C}}{\partial \bar{r}}+\frac{h^2}{D^2}\frac{\partial^2\bar{C}}{\partial \bar{z}^2}+\frac{\cos\bar{\Theta}}{D}\frac{\partial \bar{C}}{\partial \bar{r}}-\frac{\sin\bar{\Theta}}{\bar{r}D}\frac{\partial \bar{C}}{\partial \bar{\Theta}}+\frac{1}{\bar{r}^2}\frac{\partial^2\bar{C}}{\partial \bar{\Theta}^2}\right)$$
$$+Rc(\bar{C}-C_0), \tag{21}$$

Electric potential equation:

$$\left(\frac{\partial^2\tilde{\psi}_i}{\partial \bar{r}^2}+\frac{1}{\bar{r}}\frac{\partial \tilde{\psi}_i}{\partial \bar{r}}+\frac{h^2}{D^2}\frac{\partial^2\tilde{\psi}_i}{\partial \bar{z}^2}+\frac{\cos\bar{\Theta}}{D}\frac{\partial \tilde{\psi}_i}{\partial \bar{r}}-\frac{\sin\bar{\Theta}}{\bar{r}D}\frac{\partial \tilde{\psi}_i}{\partial \bar{\Theta}}+\frac{1}{\bar{r}^2}\frac{\partial^2\tilde{\psi}_i}{\partial \bar{\Theta}^2}\right)=\kappa^2\tilde{\psi}_i \tag{22}$$

Here, $\bar{I}$ denotes the viscous dissipation and its mathematical expression for blood flow of core region is given in Eq. (23)

$$\bar{I}=\;2^{\frac{q-1}{2}}\mu^{nf}K\Big[(\phi)^2_{\bar{r}\bar{r}}+(\phi)^2_{\bar{\Theta}\bar{\Theta}}+(\phi)^2_{\bar{z}\bar{z}}+2((\phi)^2_{\bar{r}\bar{\Theta}}+(\phi)^2_{\bar{\Theta}\bar{z}}+(\phi)^2_{\bar{z}\bar{r}})\Big]^q. \tag{23}$$

where, $\bar{U},\bar{V},\bar{W}$ represents the dimensional form of velocity components for blood flow in $\bar{r},\bar{\Theta},\bar{z}$ directions, respectively. Here, $\bar{T}$, Q, $\bar{C}$, and Rc indicates the dimensional form of blood flow temperature, applied heating source, concentration, and chemical reaction parameter, respectively.

Table 1. Dimensionless parameter.

$\bar{r} = R_0\tilde{r}$	$\bar{z} = L_0\tilde{z}$	$\bar{\Theta} = \tilde{\Theta}$	$\omega = \frac{u_0}{L_0}\tilde{\omega}$	$L = L_0\tilde{L}$
$d = L_0\tilde{d}$	$t = \frac{L_0}{u_0}\tilde{t}$	$R = R_0\tilde{R}$	$\bar{P} = \frac{u_0 L_0 \mu^b}{R_0^2}\tilde{P}$	$\bar{U} = \frac{\delta u_0}{L_0}\tilde{U}$
$\bar{V} = \frac{\delta u_0}{L_0}\tilde{V}$	$\bar{W} = u_0\tilde{W}$	$\tilde{\delta} = \frac{\Delta}{R_0}$	$\varepsilon = \frac{R_0}{h}$	$\tilde{\theta} = \frac{\bar{T}-T_w}{T_o-T_w}$
$\alpha = \frac{R_0}{L_0}$	$H = \frac{QR_0^2}{(T_0-T_w)K^b}$	$M = \frac{\sigma B_0^2 R_0^2}{u_0^2}$	$Re = \frac{\rho^b R_0 u_0}{\mu^b}$	$Ec = \frac{u_0^2}{C_p(T_0-T_w)}$
$Pr = \frac{C_p\mu}{K^b}$	$Br = EcPr$	$\tilde{C} = \frac{\bar{C}-C_0}{C_w-C_0}$	$Sc = \frac{\mu^b}{\rho^b Dp^b}$	$\xi = \frac{R_0^2\rho^b Rc}{\mu^b}$
$\bar{psi}_i = \frac{\Upsilon_v e\tilde{\psi}_i}{K_B T_{la}}$	$\rho_{el} = \frac{\Upsilon_v e R_0^2}{K_B T_{la}}\tilde{\rho}_{el}$	$E_s = \frac{\bar{E}_s}{E_0}$	$u_e = \frac{\Xi K_B T_{la} E_0}{\Upsilon_v e\mu^b}$	$u_r = \frac{u_e}{u_0}$

The above-mentioned dimensional form of governing and stenosis geometry equations will be transformed into the non-dimensional form using the following non-dimensional parameters mentioned in Table 1.

The dimensionless form of stenosis is considered as [40].

The table mentioned above 1 has been utilized to transform governing equations into dimensionless forms. Then after fully developed flow, mild stenosis ($\tilde{\delta} \ll 1$), and $O(1) = \alpha = \frac{R_0}{L_0}$ [41] conditions have been employed to simplify dimensionless governing equations. The simplified form of the governing equations are written as

$$\frac{\partial \tilde{P}}{\partial \tilde{r}} = 0, \tag{24}$$

$$\frac{\partial \tilde{P}}{\partial \tilde{\Theta}} = 0, \tag{25}$$

$$\begin{aligned}\frac{1}{\bar{D}}\frac{\partial \tilde{P}}{\partial \tilde{z}} = \frac{\mu^{nf}}{\mu^f}\Omega_c^*\left(\frac{\partial^2 \tilde{W}}{\partial \tilde{r}^2} + \frac{1}{\tilde{r}}\frac{\partial \tilde{W}}{\partial \tilde{r}} + \frac{1}{\tilde{r}^2}\frac{\partial^2 \tilde{W}}{\partial \tilde{\Theta}^2} - \frac{\varepsilon^2 \tilde{W}}{\bar{D}^2} + \frac{\varepsilon}{\bar{D}}\left[\cos\tilde{\Theta}\frac{\partial \tilde{W}}{\partial \tilde{r}} - \frac{\sin\tilde{\Theta}}{\tilde{r}}\frac{\partial \tilde{W}}{\partial \tilde{\Theta}}\right]\right) \\ + \frac{\mu^{nf}}{\mu^f}\left(\frac{\partial \tilde{W}}{\partial \tilde{r}} - \frac{\varepsilon \tilde{W}\cos\tilde{\Theta}}{\bar{D}}\right)\frac{\partial \Omega_c^*}{\partial \tilde{r}} + \frac{\mu^{nf}}{\mu^f}\left(\frac{1}{\tilde{r}^2}\frac{\partial \tilde{W}}{\partial \tilde{\Theta}} + \frac{\varepsilon \tilde{W}\sin\tilde{\Theta}}{\tilde{r}\bar{D}}\right)\frac{\partial \Omega_c^*}{\partial \tilde{\Theta}} + \frac{\bar{\kappa}^2 u_r E_s \varepsilon}{D}\bar{\psi}_i - M\tilde{W}\frac{\sigma^{nf}}{\sigma^f}\end{aligned} \tag{26}$$

$$\begin{aligned}\frac{\partial^2 \tilde{T}}{\partial \tilde{r}^2} + \frac{1}{\tilde{r}}\frac{\partial \tilde{T}}{\partial \tilde{r}} + \frac{\varepsilon\cos\tilde{\Theta}}{\bar{D}}\frac{\partial \tilde{T}}{\partial \tilde{r}} - \frac{\varepsilon\sin\tilde{\Theta}}{\tilde{r}\bar{D}}\frac{\partial \tilde{T}}{\partial \tilde{\Theta}} + \frac{1}{\tilde{r}^2}\frac{\partial^2 \tilde{T}}{\partial \tilde{\Theta}^2} \\ + \frac{K^b}{K^{nf}}(H + Br\ \tilde{I}) + \frac{K^f}{K^{nf}}\frac{\sigma^{nf}}{\sigma^f}(S_z E_s^2 + MBr\tilde{W}^2) = 0,\end{aligned} \tag{27}$$

$$\frac{\partial^2 \tilde{C}}{\partial \tilde{r}^2} + \frac{1}{\tilde{r}}\frac{\partial \tilde{C}}{\partial \tilde{r}} + \frac{\varepsilon\cos\tilde{\Theta}}{\bar{D}}\frac{\partial \tilde{C}}{\partial \tilde{r}} - \frac{\varepsilon\sin\tilde{\Theta}}{\tilde{r}\bar{D}}\frac{\partial \tilde{C}}{\partial \tilde{\Theta}} + \frac{1}{\tilde{r}^2}\frac{\partial^2 \tilde{C}}{\partial \tilde{\Theta}^2} - \frac{Dp^f}{Dp^{nf}}Sc\xi\tilde{C} = 0, \tag{28}$$

$$\frac{\partial^2 \bar{\psi}_i}{\partial \tilde{r}^2} + \frac{1}{\tilde{r}}\frac{\partial \bar{\psi}_i}{\partial \tilde{r}} + \frac{\varepsilon\cos\tilde{\Theta}}{\bar{D}}\frac{\partial \bar{\psi}_i}{\partial \tilde{r}} - \frac{\varepsilon\sin\tilde{\Theta}}{\tilde{r}\bar{D}}\frac{\partial \bar{\psi}_i}{\partial \tilde{\Theta}} + \frac{1}{\tilde{r}^2}\frac{\partial^2 \bar{\psi}_i}{\partial \tilde{\Theta}^2} - \bar{\kappa}^2\bar{\psi}_i = 0, \tag{29}$$

where

$$\bar{D} = 1 + \varepsilon\tilde{r}\cos\tilde{\Theta},$$

$$\Omega^* = 2^{\frac{q-1}{2}}\left[\left(-\frac{\varepsilon\tilde{W}\cos\tilde{\Theta}}{\bar{D}} + \frac{\partial \tilde{W}}{\partial \tilde{r}}\right)^2 + \left(\frac{\varepsilon\tilde{W}\sin\tilde{\Theta}}{\bar{D}} + \frac{1}{\tilde{r}}\frac{\partial \tilde{W}}{\partial \tilde{\Theta}}\right)^2\right]^{\frac{q-1}{2}},$$

$$\tilde{I} = \frac{2^{q-1}}{(1-m)^{2.5}}\left[\left(-\frac{\varepsilon\tilde{W}\cos\tilde{\Theta}}{\bar{D}} + \frac{\partial \tilde{W}}{\partial \tilde{r}}\right)^2 + \left(\frac{\varepsilon\tilde{W}\sin\tilde{\Theta}}{\bar{D}} + \frac{1}{\tilde{r}}\frac{\partial \tilde{W}}{\partial \tilde{\Theta}}\right)^2\right]^q,$$

where, M, E_s, S_z are the non-dimensional form of magnetic field, streaming potential and heat generation due to joule heating. The mathematical formulation of dimensionless boundary condition is mentioned in Eq. (30)

$$\begin{cases} \frac{\partial \tilde{W}}{\partial \tilde{r}} = 0, & \frac{\partial \tilde{T}}{\partial \tilde{r}} = 0, & \frac{\partial \tilde{C}}{\partial \tilde{r}} = 0, & \frac{\partial \bar{\psi}_i}{\partial \tilde{r}} = 0, & \text{at} \quad \tilde{r} = h'(\tilde{z}), \\ \tilde{W} = 0, & \tilde{T} = 0, & \tilde{C} = 1, & \bar{\psi}_i = \psi_w, & \text{at} \quad \tilde{r} = \tilde{R}(\tilde{z}, \tilde{t}), \\ \frac{\partial \tilde{W}}{\partial \tilde{\Theta}} = 0, & \frac{\partial \tilde{T}}{\partial \tilde{\Theta}} = 0, & \frac{\partial \tilde{C}}{\partial \tilde{\Theta}} = 0, & \frac{\partial \bar{\psi}_i}{\partial \tilde{\Theta}} = 0, & \text{at} \quad \tilde{\Theta} = 0 \ \& \ \tilde{\Theta} = \pi, \end{cases} \tag{30}$$

2.5. Streaming potential and EKEC

Ding et al. [5] calculated the streaming potential for the cured microtube using the perturbation technique. To calculate streaming potential, firstly they introduced ionic current and its expression is

$$I_{ion} = I_s + I_c = -2n_0 e \mathrm{Y}_v R_0^2 u_0 \left(\int_0^{\pi} \int_0^{\tilde{R}(\tilde{z},\tilde{t})} \bar{\psi}_i \tilde{W} \tilde{r} d\tilde{r} d\tilde{\Theta} + M_p u_r E_s \int_0^{\pi} \int_0^{\tilde{R}(\tilde{z},\tilde{t})} \frac{\tilde{r}}{\bar{D}} d\tilde{r} d\tilde{\Theta} \right) \tag{31}$$

where, M_p represents the dimensional conduction current (inverse of ionic Peclet number)

The analytical form of the streaming potential is

$$E_s = -\frac{\int_0^{\pi} \int_0^{\tilde{R}(\tilde{z},\tilde{t})} \bar{\psi}_i \tilde{W} \tilde{r} d\tilde{r} d\tilde{\Theta}}{M_p u_r E_s \int_0^{\pi} \int_0^{\tilde{R}(\tilde{z},\tilde{t})} \frac{\tilde{r}}{\bar{D}} d\tilde{r} d\tilde{\Theta}} \tag{32}$$

Under the pressure-driven flow assumption, the conversion of mechanical and chemical energy produced by streaming potential and EDL, into the electric energy is called EKEC. The energy conversion efficiency have vital roles in fluid flow through micro-tubes, therefore EKEC efficiency in curved artery is follows as [11,42]

$$\bar{\chi} = \frac{\bar{P}_o}{\bar{P}_i} \tag{33}$$

where, $\bar{P}_o$ and $\bar{P}_i$ are called the output and input power of the curved artery and defined as

$$\bar{P}_i = |-\frac{h}{D}\frac{\partial \bar{P}}{\partial \bar{z}} Q| \tag{34}$$

$$\bar{P}_o = \frac{1}{4}|I_s E_s| \tag{35}$$

where Q known as volumetric flow rate.

3. Procedure of solution

With the use of the aforementioned non-dimensional boundary conditions, a computational process to obtain a solution of highly non-linear PDEs (24)–(29) (dimensionless governing equations) has been performed using the Finite difference method [29].

The central difference formula of the second order has been employed to discretized the spatial derivatives in the uniform mesh size for the domain $[0 \quad \tilde{R}(\tilde{z}, \tilde{t})] \times [o \quad \pi]$. Discretization of derivatives can be performed using the given process in Eq. (36)

$$\begin{cases} \dfrac{\partial G_s}{\partial \tilde{r}} = \dfrac{(G_s)_{x+1,y} - (G_s)_{x-1,y}}{2\Delta r}, \\ \dfrac{\partial G_s}{\partial \tilde{\Theta}} = \dfrac{(G_s)_{x,y+1} - (G_s)_{x,y-1}}{2\Delta\Theta}, \\ \dfrac{\partial^2 G_s}{\partial \tilde{r}^2} = \dfrac{(G_s)_{x+1,y} - 2(G_s)_{x,y} + (G_s)_{x-1,y}}{(\Delta r)^2}, \\ \dfrac{\partial^2 G_s}{\partial \tilde{\Theta}^2} = \dfrac{(G_s)_{x,y+1} - 2(G_s)_{x,y} + (G_s)_{x,y-1}}{(\Delta\Theta)^2}. \end{cases} \tag{36}$$

Here, G_s represents the velocity, temperature, concentration, and potential term for blood flow.

In the present mathematical study Δr and $\Delta\Theta$ represents the uniform mesh size in $\tilde{r}$ and $\tilde{\Theta}$ direction, respectively. The mathematical expression for Δr and $\Delta\Theta$ are as follows- $\Delta r = \frac{\tilde{R}(\tilde{z},\tilde{t})}{L_1 - 1}$ and $\Delta\Theta = \frac{\pi}{L_2 - 1}$ where L_1 and L_2 denote the total number of mesh points in $\tilde{r}$ & $\tilde{\Theta}$ directions.

The discretization of these governing equations will be

$$\begin{aligned} \frac{1}{\bar{D}_{x,y}}\left(\frac{\partial \tilde{P}}{\partial \tilde{z}}\right)_{x,y} = {} & \frac{\mu^{nf}}{\mu^{f}}(\Omega^*)_{x,y}\left(\frac{(\tilde{W})_{x+1,y} - 2(\tilde{W})_{x,y} + (\tilde{W})_{x-1,y}}{(\Delta r)^2} + \frac{1}{\tilde{r}_x}\frac{(\tilde{W})_{x+1,y} - (\tilde{W})_{x-1,y}}{2\Delta r}\right. \\ & + \frac{1}{\tilde{r}_x^2}\frac{(\tilde{W})_{x,y+1} - 2(\tilde{W})_{x,y} + (\tilde{W})_{x,y-1}}{(\Delta\Theta)^2} - \frac{\varepsilon^2(\tilde{W})_{x,y}}{\bar{D}_{x,y}^2} \\ & \left. + \frac{\varepsilon}{\bar{D}_{x,y}}\left[\cos\tilde{\Theta}_y \frac{(\tilde{W})_{x+1,y} - (\tilde{W})_{x-1,y}}{2\Delta r} - \frac{\sin\tilde{\Theta}_y}{\tilde{r}_x}\frac{(\tilde{W})_{x,y+1} - (\tilde{W})_{x,y-1}}{2\Delta\Theta}\right]\right) \\ & + \frac{\mu^{nf}}{\mu^{f}}\left(\frac{(\tilde{W})_{x+1,y} - (\tilde{W})_{x-1,y}}{2\Delta r} - \frac{\varepsilon(\tilde{W})_{x,y}\cos\tilde{\Theta}_y}{\bar{D}_{x,y}}\right) \\ & \frac{(\Omega^*)_{x+1,y} - (\Omega^*)_{x-1,y}}{2\Delta r} + \frac{\mu^{nf}}{\mu^{f}}\left(\frac{1}{\tilde{r}_x^2}\frac{(\tilde{W})_{x,y+1} - (\tilde{W})_{x,y-1}}{2\Delta\Theta} + \frac{\varepsilon(\tilde{W})_{x,y}\sin\tilde{\Theta}_y}{\tilde{r}_x\bar{D}_{x,y}}\right)\frac{(\Omega^*)_{x,y+1} - (\Omega^*)_{x,y-1}}{2\Delta\Theta} \\ & + \frac{\bar{\kappa}^2 u_r (E_s)_{x,y}\varepsilon}{\bar{D}_{x,y}}(\bar{\psi}_i)_{x,y} - M(\tilde{W})_{x,y}\frac{\sigma^{nf}}{\sigma^{f}}, \end{aligned} \tag{37}$$

$$\begin{aligned} & \frac{(\tilde{T})_{x+1,y} - 2(\tilde{T})_{x,y} + (\tilde{T})_{x-1,y}}{(\Delta r)^2} + \frac{1}{\tilde{r}_x}\frac{(\tilde{T})_{x+1,y} - (\tilde{T})_{x-1,y}}{2\Delta r} + \frac{\varepsilon\cos\tilde{\Theta}_y}{\bar{D}_{x,y}}\frac{(\tilde{T})_{x+1,y} - (\tilde{T})_{x-1,y}}{2\Delta r} - \frac{\varepsilon\sin\tilde{\Theta}_y}{\tilde{r}_x\bar{D}_{x,y}} \\ & \frac{(\tilde{T})_{x,y+1} - (\tilde{T})_{x,y-1}}{2\Delta\Theta} + \frac{1}{\tilde{r}_x^2}\frac{(\tilde{T})_{x,y+1} - 2(\tilde{T})_{x,y} + (\tilde{T})_{x,y-1}}{(\Delta\Theta)^2} = -\frac{K^b}{K^{nf}}(H + Br\ (\tilde{I})_{x,y}) \\ & - \frac{K^f}{K^{nf}}\frac{\sigma^{nf}}{\sigma^f}(S_z(E_s^2)x,y + MBr(\tilde{W}^2)_{x,y}) \end{aligned} \tag{38}$$

$$\begin{aligned} & \frac{(\tilde{C})_{x+1,y} - 2(\tilde{C})_{x,y} + (\tilde{C})_{x-1,y}}{(\Delta r)^2} + \frac{1}{\tilde{r}_x}\frac{(\tilde{C})_{x+1,y} - (\tilde{C})_{x-1,y}}{2\Delta r} + \frac{\varepsilon\cos\tilde{\Theta}_y}{\bar{D}_{x,y}}\frac{(\tilde{C})_{x+1,y} - (\tilde{C})_{x-1,y}}{2\Delta r} - \frac{\varepsilon\sin\tilde{\Theta}_y}{\tilde{r}_x\bar{D}_{x,y}} \\ & \frac{(\tilde{C})_{x,y+1} - (\tilde{C})_{x,y-1}}{2\Delta\Theta} + \frac{1}{\tilde{r}_x^2}\frac{(\tilde{C})_{x,y+1} - 2(\tilde{C})_{x,y} + (\tilde{C})_{x,y-1}}{(\Delta\Theta)^2} - \frac{Dp^f}{Dp^{nf}}Sc\xi(\tilde{C})_{x,y} = 0, \end{aligned} \tag{39}$$

$$\frac{(\bar{\psi}_i)_{x+1,y}-2(\bar{\psi}_i)_{x,y}+(\bar{\psi}_i)_{x-1,y}}{(\Delta r)^2}+\frac{1}{\tilde{r}_x}\frac{(\bar{\psi}_i)_{x+1,y}-(\bar{\psi}_i)_{x-1,y}}{2\Delta r}+\frac{\varepsilon\cos\tilde{\Theta}_y}{\bar{D}_{x,y}}\frac{(\bar{\psi}_i)_{x+1,y}-(\bar{\psi}_i)_{x-1,y}}{2\Delta r}-\frac{\varepsilon\sin\tilde{\Theta}_y}{\tilde{r}_x\bar{D}_{x,y}}$$
$$\frac{(\bar{\psi}_i)_{x,y+1}-(\bar{\psi}_i)_{x,y-1}}{2\Delta\Theta}+\frac{1}{\tilde{r}_x^2}\frac{(\bar{\psi}_i)_{x,y+1}-2(\bar{\psi}_i)_{x,y}+(\bar{\psi}_i)_{x,y-1}}{(\Delta\Theta)^2}-\bar{\kappa}^2(\bar{\psi}_i)_{x,y}=0, \tag{40}$$

where $\bar{D}_{x,y}=1+\varepsilon\tilde{r}_x\cos\tilde{\Theta}_y$,

$$(\Omega^*)_{x,y}=2^{\frac{q-1}{2}}\left[\left(-\frac{\varepsilon(\tilde{W})_{x,y}\cos\tilde{\Theta}_y}{\bar{D}_{x,y}}+\frac{(\tilde{W})_{x+1,y}-(\tilde{W})_{x-1,y}}{2\Delta r}\right)^2+\left(\frac{\varepsilon(\tilde{W})_{x,y}\sin\tilde{\Theta}_y}{\bar{D}_{x,y}}+\frac{1}{\tilde{r}_x}\frac{(\tilde{W})_{x,y+1}-(\tilde{W})_{x,y-1}}{2\Delta\Theta}\right)\ 2\right]^{\frac{q-1}{2}},$$
$$(\tilde{I})_{x,y}=2^{q-1}\left[\left(-\frac{\varepsilon(\tilde{W})_{x,y}\cos\tilde{\Theta}_y}{\bar{D}_{x,y}}+\frac{(\tilde{W})_{x+1,y}-(\tilde{W})_{x-1,y}}{2\Delta r}\right)^2+\left(\frac{\varepsilon(\tilde{W})_{x,y}\sin\tilde{\Theta}_y}{\bar{D}_{x,y}}+\frac{1}{\tilde{r}_x}\frac{(\tilde{W})_{x,y+1}-(\tilde{W})_{x,y-1}}{2\Delta\Theta}\right)^2\right]^q,$$

According to published research work [43,44], due to pumping of heart, blood flow reflect its pulsatile nature of flow. Therefore, the mathematical formulation of pressure gradient can be written as

$$\frac{\partial\tilde{P}}{\partial\tilde{z}}=P_0e^{-\kappa\Omega t}. \tag{41}$$

Since the above-mentioned non-dimensional governing equations non-dimensional governing equations can be reduced into 2D non-linear PDEs. With the discretization of these PDEs, a five-band system of non-linear algebraic equations have been obtained.

$$AX=b.$$

where A is coefficient matrix.

The system is highly non-linear; therefore, solving it using the Gaussian elimination method is not feasible.

Stone's strongly implicit method [30] has been employed to solve the system of non-linear equations. A global nodal index k has been assigned for every mesh point.

$$k=(y-1)*L_1+x.$$

Further, we will re-frame the discretized non-dimensional governing equations by assigning a unique nodel index $k=(y-1)*L_1+x$.

$$\begin{aligned}\frac{1}{\bar{D}_k}\left(\frac{\partial\tilde{P}}{\partial\tilde{z}}\right)_k=&\frac{\mu^{nf}}{\mu^f}(\Omega^*)_k\left(\frac{(\tilde{W})_{k+1}-2(\tilde{W})_k+(\tilde{W})_{k-1}}{(\Delta r)^2}+\frac{1}{\tilde{r}_k}\frac{(\tilde{W})_{k+1}-(\tilde{W})_{k-1}}{2\Delta r}\right.\\&+\frac{1}{\tilde{r}_k^2}\frac{(\tilde{W})_{k+L_1}-2(\tilde{W})_k+(\tilde{W})_{k-L_1}}{(\Delta\Theta)^2}-\frac{\varepsilon^2(\tilde{W})_k}{\bar{D}_k^2}\\&\left.+\frac{\varepsilon}{\bar{D}_k}\left[\cos\tilde{\Theta}_k\frac{(\tilde{W})_{k+1}-(\tilde{W})_{k-1}}{2\Delta r}-\frac{\sin\tilde{\Theta}_k}{\tilde{r}_k}\frac{(\tilde{W})_{k+L_1}-(\tilde{W})_{k-L_1}}{2\Delta\Theta}\right]\right)\\&+\frac{\mu^{nf}}{\mu^f}\left(\frac{(\tilde{W})_{k+1}-(\tilde{W})_{k-1}}{2\Delta r}-\frac{\varepsilon(\tilde{W})_k\cos\tilde{\Theta}_k}{\bar{D}_k}\right)\\&\frac{(\Omega^*)_{k+1}-(\Omega^*)_{k-1}}{2\Delta r}+\frac{\mu^{nf}}{\mu^f}\left(\frac{1}{\tilde{r}_k^2}\frac{(\tilde{W})_{k+L_1}-(\tilde{W})_{k-L_1}}{2\Delta\Theta}+\frac{\varepsilon(\tilde{W})_k\sin\tilde{\Theta}_k}{\tilde{r}_k\bar{D}_k}\right)\frac{(\Omega^*)_{k+L_1}-(\Omega^*)_{k-L_1}}{2\Delta\Theta}\\&+\frac{\bar{\kappa}^2u_r(E_s)_k\varepsilon}{\bar{D}_k}(\bar{\psi}_i)_k-M(\tilde{W})_k\frac{\sigma^{nf}}{\sigma^f},\end{aligned} \tag{42}$$

$$\frac{(\tilde{T})_{k+1}-2(\tilde{T})_k+(\tilde{T})_{k-1}}{(\Delta r)^2}+\frac{1}{\tilde{r}_k}\frac{(\tilde{T})_{k+1}-(\tilde{T})_{k-1}}{2\Delta r}+\frac{\varepsilon\cos\tilde{\Theta}_k}{\bar{D}_k}\frac{(\tilde{T})_{k+1}-(\tilde{T})_{k-1}}{2\Delta r}-\frac{\varepsilon\sin\tilde{\Theta}_k}{\tilde{r}_k\bar{D}_k}$$
$$\frac{(\tilde{T})_{k+L_1}-(\tilde{T})_{k-L_1}}{2\Delta\Theta}+\frac{1}{\tilde{r}_k^2}\frac{(\tilde{T})_{k+L_1}-2(\tilde{T})_k+(\tilde{T})_{k-L_1}}{\left((\Delta\Theta)^2=-\frac{K^b}{K^{nf}}\left(H+Br\ (\tilde{I})_k\right)-\frac{K^f}{K^{nf}}\frac{\sigma^{nf}}{\sigma^f}(S_z(E_s^2)k+MBr(\tilde{W}^2)_k\right)} \tag{43}$$

$$\frac{(\tilde{C})_{k+1}-2(\tilde{C})_k+(\tilde{C})_{k-1}}{(\Delta r)^2}+\frac{1}{\tilde{r}_k}\frac{(\tilde{C})_{k+1}-(\tilde{C})_{k-1}}{2\Delta r}+\frac{\varepsilon\cos\tilde{\Theta}_k}{\bar{D}_k}\frac{(\tilde{C})_{k+1}-(\tilde{C})_{k-1}}{2\Delta r}-\frac{\varepsilon\sin\tilde{\Theta}_k}{\tilde{r}_k\bar{D}_k}$$
$$\frac{(\tilde{C})_{k+L_1}-(\tilde{C})_{k-L_1}}{2\Delta\Theta}+\frac{1}{\tilde{r}_k^2}\frac{(\tilde{C})_{k+L_1}-2(\tilde{C})_k+(\tilde{C})_{k-L_1}}{(\Delta\Theta)^2}-\frac{Dp^f}{Dp^{nf}}Sc\xi(\tilde{C})_k=0, \tag{44}$$

$$\frac{(\bar{\psi}_i)_{k+1}-2(\bar{\psi}_i)_k+(\bar{\psi}_i)_{k-1}}{(\Delta r)^2}+\frac{1}{\tilde{r}_k}\frac{(\bar{\psi}_i)_{k+1}-(\bar{\psi}_i)_{k-1}}{2\Delta r}+\frac{\varepsilon\cos\tilde{\Theta}_k}{\bar{D}_k}\frac{(\bar{\psi}_i)_{k+1}-(\bar{\psi}_i)_{k-1}}{2\Delta r}-\frac{\varepsilon\sin\tilde{\Theta}_k}{\tilde{r}_k\bar{D}_k}$$
$$\frac{(\bar{\psi}_i)_{k+L_1}-(\bar{\psi}_i)_{k-L_1}}{2\Delta\Theta}+\frac{1}{\tilde{r}_k^2}\frac{(\bar{\psi}_i)_{k+L_1}-2(\bar{\psi}_i)_k+(\bar{\psi}_i)_{k-L_1}}{(\Delta\Theta)^2}-\bar{\kappa}^2(\bar{\psi}_i)_k=0, \tag{45}$$

After allocating the global nodal index, the coefficient matrix [A] will be factorized into lower and upper triangular matrices. After factorized matrix [A], the residual will be computed. Further, backward and forward substitution will be employed to find a solution. This iterative process is repeated until the residual becomes lesser than the desirable error tolerance. Stone's method is used for inner iteration, then Newton's scheme is applied for outer iteration. For each inner and outer iteration, the absolute error tolerance of 10^{-6} is taken into account.

$$[A]X=[L][U]X=b.$$

After numerically computed the velocity and temperature, some important physical phenomena, such as wall shear stress, Nusselt number, and flow rate profiles can be calculated using numerical velocity and temperature profile data.

The Flow rate Q, frictional impedance λ, and wall shear stress τ_w can be calculated as follows

$$Q=\int_0^{\tilde{R}(\tilde{z},\tilde{t})}\int_0^{\pi}\tilde{r}\tilde{W}(\tilde{r},\tilde{\Theta},\tilde{z})d\tilde{r}d\tilde{\Theta}, \tag{46}$$

$$\lambda=\frac{\int_0^L\left(-\frac{\partial\tilde{P}}{\partial\tilde{z}}\right)d\tilde{z}}{Q}, \tag{47}$$

$$\tau_w=-\frac{\mu^{nf}}{\mu^b}2^{\frac{q-1}{2}}\left(\frac{\partial\tilde{W}}{\partial\tilde{r}}\right)^q_{\tilde{r}=\tilde{R}(\tilde{z},\tilde{t})}, \tag{48}$$

The Mathematical calculation of Nusselt number can performed as

$$Nu=-\frac{K^{nf}}{K^b}\left(\frac{\partial\tilde{T}}{\partial\tilde{r}}\right)_{\tilde{r}=\tilde{R}(\tilde{z},\tilde{t})}. \tag{49}$$

4. Entropy generation and irreversibility

Entropy generation is critical for understanding biological thermodynamics in blood flow through constricted regions. By considering above mentioned conditions, the general form of entropy generation can be written as follows [45–47]

$$E^{gen} = \underbrace{\frac{K^{nf}(\nabla T)^2}{T_w^2}}_{\text{Thermal irreversibility}} + \underbrace{\frac{I}{T_w}}_{\text{Fluid friction irrversibility}} + \underbrace{\frac{\vec{J}\cdot\vec{J}}{T_w\sigma^{nf}}}_{\text{Joule heating irreversibility}} + \underbrace{\frac{Dp^{nf}(\nabla C)^2}{C_w}}_{\text{Solute irreversibility}}, \tag{50}$$

The present study does not include the irreversibility process which occurs due to chemical reaction. The following are the mathematical formulae to estimate the amount of entropy generation in both regions:

$$\bar{E}^{gen} = \underbrace{\frac{K^{nf}}{\bar{T}_w^2}\left[\left(\frac{\partial\bar{T}}{\partial\bar{r}}\right)^2 + \left(\frac{1}{\bar{r}}\frac{\partial\bar{T}}{\partial\Theta}\right)^2 + \left(\frac{h}{D}\frac{\partial\bar{T}}{\partial\bar{z}}\right)^2\right]}_{\text{Thermal irreversibility}} + \underbrace{\frac{\bar{I}}{\bar{T}_w}}_{\text{Fluid friction irrversibility}} + \underbrace{\frac{\vec{J}\cdot\vec{J}}{T_w\sigma^{nf}}}_{\text{Joule heating irreversibility}} + \underbrace{\frac{Dp^{nf}}{\bar{C}_w^2}\left[\left(\frac{\partial\bar{C}}{\partial\bar{r}}\right)^2 + \left(\frac{1}{\bar{r}}\frac{\partial\bar{C}}{\partial\Theta}\right)^2 + \left(\frac{h}{D}\frac{\partial\bar{C}}{\partial\bar{z}}\right)^2\right]}_{\text{Solute irreversibility}}, \tag{51}$$

Eq. (51) will be converted into the dimensionless form by using Table 1 and considering above mentioned flow conditions

$$\tilde{E}^{gen} = \frac{\bar{E}^{gen}}{\bar{E}}, \bar{E}^{gen} = \frac{K^{nf}}{K^b}\left[\left(\frac{\partial\tilde{T}}{\partial\tilde{r}}\right)^2 + \left(\frac{1}{\tilde{r}}\frac{\partial\tilde{T}}{\partial\tilde{\Theta}}\right)^2\right] + \frac{Br}{A}\tilde{I} + \frac{\sigma^{nf}}{\sigma^b}\frac{1}{A}\left[S_z E_s^2 + MBr\tilde{W}^2\right] + \frac{Dp^{nf}}{Dp^b}\frac{\Gamma\Lambda}{A}\left[\left(\frac{\partial\tilde{C}}{\partial\tilde{r}}\right)^2 + \left(\frac{1}{\tilde{r}}\frac{\partial\tilde{C}}{\partial\tilde{\Theta}}\right)^2\right], \tag{52}$$

where $E = \frac{K_p(\bar{T}_0 - T_w)^2}{T_w^2 R_0^2}, A = \frac{\bar{T}_0 - T_w}{T_w}$.

The discretization of entropy generation equation is

$$\begin{aligned}(\bar{E}^{gen})_{x,y} &= \frac{K^{nf}}{K^b}\left[\left(\frac{(\tilde{T})_{x+1,y} - (\tilde{T})_{x-1,y}}{2\Delta r}\right)^2 + \left(\frac{1}{\tilde{r}_x}\frac{(\tilde{T})_{x,y+1} - (\tilde{T})_{x,y-1}}{2\Delta\Theta}\right)^2\right] + \frac{Br}{A}(\tilde{I})_{x,y} \\ &+ \frac{\sigma^{nf}}{\sigma^b}\frac{1}{A}\left[S_z(E_s)^2_{x,y} + MBr(\tilde{W})^2_{x,y}\right] + \frac{Dp^{nf}}{Dp^b}\frac{\Gamma\Lambda}{A}\left[\left(\frac{(\tilde{C})_{x+1,y} - (\tilde{C})_{x-1,y}}{2\Delta r}\right)^2\right. \\ &\left.+ \left(\frac{1}{\tilde{r}_x}\frac{(\tilde{C})_{x,y+1} - (\tilde{C})_{x,y-1}}{2\Delta\Theta}\right)^2\right],\end{aligned} \tag{53}$$

Further, this discretized equation will be re-framed using unique nodel index $k = (y-1) * L_1 + x$.

$$\begin{aligned}(\bar{E}^{gen})_k &= \frac{K^{nf}}{K^b}\left[\left(\frac{(\tilde{T})_{k+1} - (\tilde{T})_{k-1}}{2\Delta r}\right)^2 + \left(\frac{1}{\tilde{r}_k}\frac{(\tilde{T})_{k+L_1} - (\tilde{T})_{k-L_1}}{2\Delta\Theta}\right)^2\right] + \frac{Br}{A}(\tilde{I})_k + \frac{\sigma^{nf}}{\sigma^b}\frac{1}{A}\left[S_z(E_s)_k^2\right. \\ &\left.+ MBr(\tilde{W})_k^2\right] + \frac{Dp^{nf}}{Dp^b}\frac{\Gamma\Lambda}{A}\left[\left(\frac{(\tilde{C})_{k+1} - (\tilde{C})_{k-1}}{2\Delta r}\right)^2 + \left(\frac{1}{\tilde{r}_k}\frac{(\tilde{C})_{k+L_1} - (\tilde{C})_{k-L_1}}{2\Delta\Theta}\right)^2\right],\end{aligned} \tag{54}$$

5. Results and discussion

A numerical research study of blood flow through an overlapped stenosed curved artery has been carried out to investigate the influence of various physical parameters, such as a magnetic field, inverse Debye length (inverse EDL thickness), heat source, flow behavior index (power-law fluid), and so on. The thermal properties of gold nanoparticles have been taken into account in this study. Therefore, nanoparticle volume fraction and their size effects have also been examined for

Table 2. Physical parameters numeric range with references.

Parameters	Ranges	Sources
Magnetic field (M)	0–8	[49,50]
Flow behavior index (q)	0.7–1.25	[37,51]
Heat source parameter (H)	0–4	[40]
Brinkman number (Br)	0.1–3	[40,52]
Inverse Debye length ($\bar{\kappa}$)	1–10	[53,54]
Schmidt number (Sc)	0.5–1.5	[50,55]
Chemical reaction parameter (ξ)	0.5–2	[40,50]

Table 3. Thermophysical properties of blood and gold nanoparticle (Au) [56,57].

Thermophysical parameter	Blood	Au
Density	1,063	19,300
Heat capacity	3,594	129
Thermal conductivity	.492	318
Electrical conductivity	.667	4.52×10^{7}
Thermal expansion coefficient	1.8×10^{-6}	1.42×10^{-5}

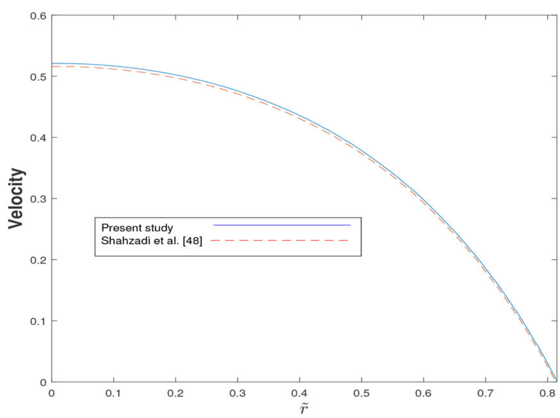

Figure 4. Validation of present investigation.

Table 4. Default values of non-dimensional parameters.

$\varepsilon = 0.1$	$M = 2$	$P_0 = 2$	$m = 0.05$	$q = 0.75$	$\bar{\kappa} = 1$	$H = 1$
$Br = 0.3$	$Sc = 1$	$\xi = 1.5$	$S_z = 1$	$\psi_w = 1$	$u_r = 1$	$M_p = 1.5$
$\Lambda = 0.8$	$\Gamma = 0.5$	$A = 0.5$				

various important physical phenomena. The study of entropy generation, energy conversion, and streaming potential (electric potential) have also been performed to make this study more realistic and impactful. The properties of power-law fluid have been considered for blood flow. The second-order finite difference method has been introduced to discretized non-dimensional governing equations. The flow domain is discretized uniformly for both ($\tilde{r}$) & ($\tilde{\Theta}$) directions. The step size in both directions is assumed $\Delta r = \Delta\Theta = 0.001$. After discretization, to obtain flow velocity, temperature, concentration, and electric potential profiles, these systems of non-linear governing equations are computed using Stone's strongly implicit method. The error tolerance for both inner and outer iterations is set up 10^{-6}. The MATLAB codes for Stones scheme have been developed to demonstrate the graphical behavior of various physical quantities, such as velocity, temperature, concentration, WSS, electric potential, heat transfer rate, entropy generation, EKEC efficiency, etc. Table 2 provides the default values for different physical parameters and their

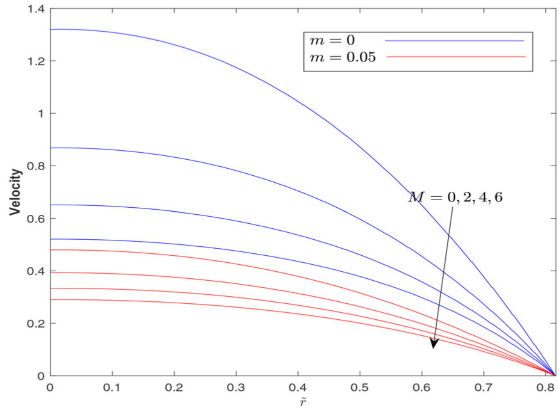

Figure 5. Velocity profile for *M* and *m*.

source of references. The thermophysical properties of blood and nanoparticle (Fe_3O_4) have been written in Table 3.

Figure 4 illustrates the validation of the current research work's mathematical model formulation and the adopted computational method's accuracy. This validation is made with the published work [48] under some assumptions. Under this assumption, the effects of the magnetic field, electric potential, and nanoparticle size effect have been ignored in our model, and the consideration of a catheter has been neglected in Shahzadi and Ijaz [48] observation. This validation process has been performed by considering the perturbation technique for [48] work and Stone's method for the present work. Figure 4 replicates the fair agreement between the present study and [48] observations.

Table 4 contains the default values of non-dimensional parameters which are used in the simulations.

The presence of hemoglobin, cell membranes, and complex structural interactions between proteins in the blood make it a biomagnetic fluid. The main protein in RBCs is hemoglobin, which contains iron particles and transports oxygen from the lungs to other body parts, such as the brain, muscles, etc. The hemoglobin structure is more sensitive to its oxygen-carrying situation and shows a significant structural variation in both oxygen-carrying and non-carrying conditions. Therefore, motivated by the blood's magnetic properties, a comparative computational study has been performed to illustrate the significance of a magnetic field applied to a stenosed curved artery. Figure 5 depicts the effect of different magnetic field intensities on the blood flow velocity. This study states that, when an external magnetic field is applied perpendicular to its axial (flow) direction, it generates a strong electromotive force known as the Lorentz force, which leads to enhanced blood flow viscosity. Consequently, a notable drop in blood flow velocity has been noticed whenever magnetic field intensity increases. It is also worth noting that the flow velocity reduction rate decreases as the value of M increases. A comparison study to describe the significance of nanoparticles (gold Au) on the stenosed artery has also been conducted using the above-mentioned figure. The properties of nanoparticles state that they are more thermally conductive than blood, but they are also highly viscous. As a result, when nanoparticles are added to the base fluid (blood), the viscosity of the nanofluid (blood-Au) increases proportionally to the amount of Au volume fraction added to the blood. This increased viscosity leads to a decay in flow velocity. Since nanoparticles can traverse through the stenosis and mend artery walls, which blood cells are unable to do, these characteristics of nanoparticles are exploited in the treatment of arteriosclerosis. Also, nanoparticles are used to diagnose various severe diseases, such as cancer cells, fungal infections, hypercholesterolemia, etc. [13].

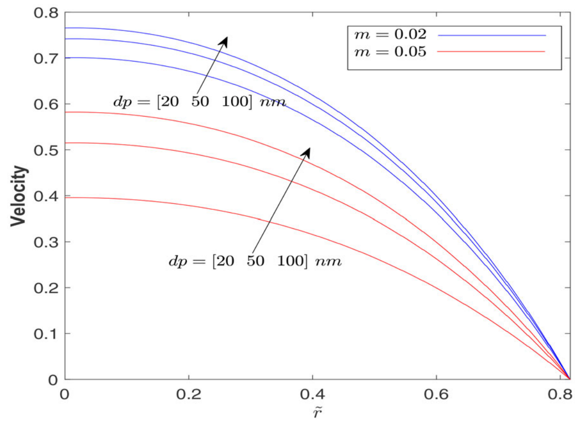

Figure 6. Velocity profile for *dp* and *m*.

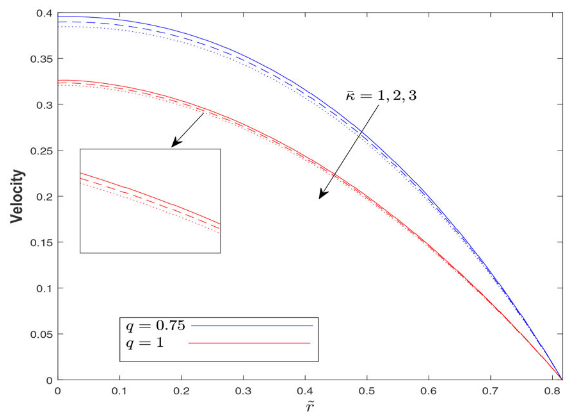

Figure 7. Velocity profile for $\bar{\kappa}$ and *q*.

The investigation of the effects of nanoparticle size and volume fraction on fluid phenomena has become a very interesting research topic in the field of bionanotechnology. Therefore, in this discussion, we used the Corcione model [34], which discusses the nanoparticle diameter effects on the flow. Figure 6 depicts the effect of gold nanoparticle diameter on blood velocity through a curved artery. According to this study, for a fixed amount of nanoparticle concentration, blood flow velocity increases as particle diameter increases. This is happening because the number of nanoparticles is higher when they are small in size, so they can easily bind up with blood cells and travel everywhere in artery, resultant blood cells become more viscous. If we increase the size of nanoparticle, there is a reduction in viscosity and increment in the velocity as observed by Corcione [34]. It is also noted that the variation in flow velocity increases with increasing nanoparticle concentration for different nanoparticle sizes.

In the electro-kinetic field, the Debye length plays an important role in electric potential distribution and flow velocity under the external electric field condition. Figure 7 depicts the effect of electro-kinetic width (inverse Debye length) on flow velocity. An increase in Debye length leads to an increase in ions quantity, which is far from the charged surface and that is used to counter the surface-charged ions. As a result, electric potential decreases. Therefore, with the increase in electro-kinetic width (inverse Debye length), the flow velocity also decreases. This article also compares Newtonian and non-Newtonian fluid properties in terms of a flow behavior index for blood flow velocity. In this case, $q < 1$ represents blood behavior as pseudoplastic

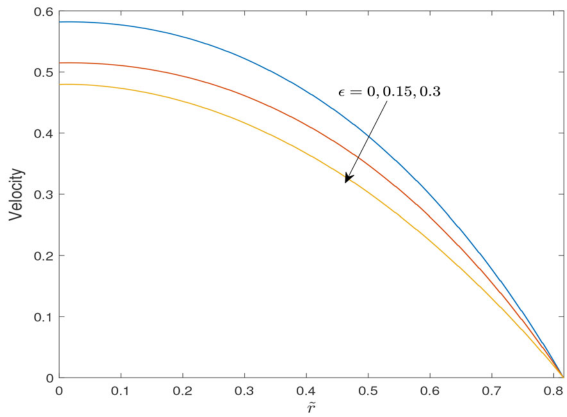

Figure 8. Velocity profile for arterial curvature (ε).

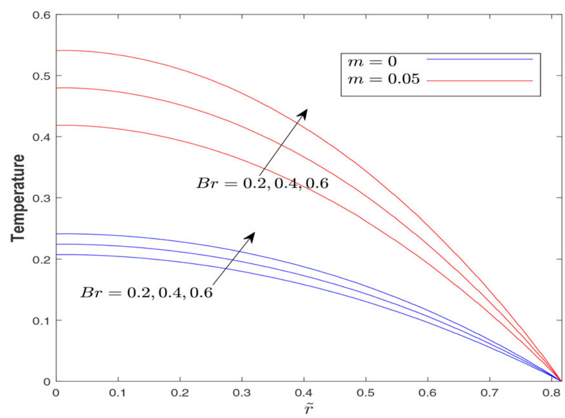

Figure 9. Temperature profile for *Br* and *m*.

(shear-thinning), $q = 1$, and Newtonian. The figure reveals that, as the value of the flow behavior index increases, the blood flow velocity decreases in the whole artery. Therefore, in a realistic situation, assuming that blood has a pseudoplastic nature will be good for the mathematical model to get an accurate result to predict disease conditions. The authors decided to consider the pseudoplastic ($q < 1$) behavior of blood whenever blood is assumed to be non-Newtonian in this computational research work based on the published literature [51] and the fruitful obtained results for flow velocity.

The blood flow velocity for various values of arterial curvature has been computed numerically, and findings are shown in Figure 8 to make the current study more realistic from the perspective of the human body. This study suggested that blood flow velocity decreases significantly with the value of arterial curvature (ε). Therefore, it can be concluded that lipid deposition chances are higher in the arteries which have high curvature due to slow fluid motion. The obtained results for the arterial curvature are in good agreement with the published work of Zaman et al. and Mekheimer and El Kot [17,59].

From the point of view of a clinical researcher, figuring out how much heat is conducted from the artery is a very important area of study. Therefore, this work distinguishes the dominance between viscous dissipation and external heating for how much heat is conducted from the artery in terms of the Brinkmann number *Br*. For fixed external heating, a positive increment in the value of the Brinkmann number leads to a decay in heat conduction from the arterial wall to the

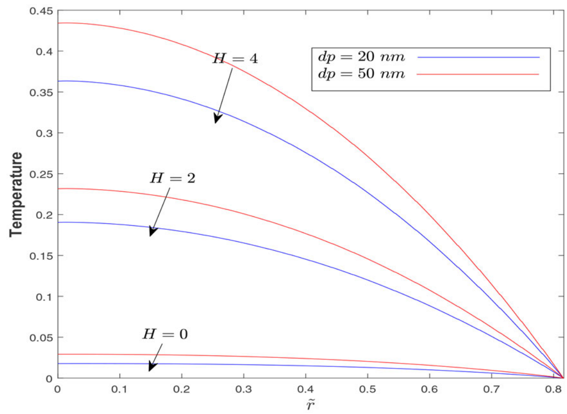

Figure 10. Temperature profile for *H* and *dp*.

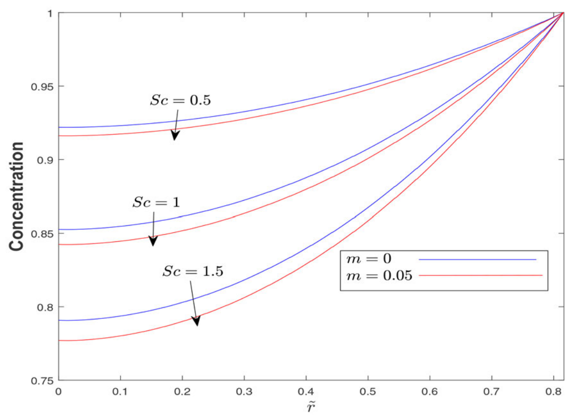

Figure 11. Concentration profile for *Sc* and *m*.

environment. In other words, it can also be said that, for fixed external heat, the generation of thermal energy by viscous dissipation is the same, but its conduction from arterial fluid to the environment is reduced. As a result, as the value of the Brinkmann number increases, the temperature of the arterial flow rises significantly, as illustrated in Figure 9. This study also describes the role of gold nanoparticles on blood flow temperature. It is well-known from the literature that gold nanoparticles are ~650 times more thermally conductive than blood. Therefore, when a small amount of gold nanoparticles is added to the blood flow, it increases its thermal conductivity significantly. As a result, the temperature of the blood flow rises. From the figure, it can also be observed that the variation in the flow temperature profile for different Brinkmann number values becomes high when nanoparticles are added to it. This is happening because small-sized nanoparticles easily bind with blood cells and generate more thermal energy in the form of viscous dissipation.

In thermal therapies, external heating is very helpful for healing serious diseases like synovial bursitis, muscle pain, killing cancer cells, osteoporosis, and so on. Therefore, the effects of external heating on the overlapped stenotic arterial flow in the presence of nanoparticles have been numerically analyzed, and the results are shown in Figure 10. This study reveals that, for a fixed Brinkmann number (i.e. fixed heat generation by viscous dissipation), the heat conduction rate from the environment to arterial blood flow increases with the increase in the heat source value. As a result, a significant boost in blood temperature is observed with the increase in the value of *H*. This study also suggests that for a fixed amount of nanoparticle volume fraction, a larger-sized

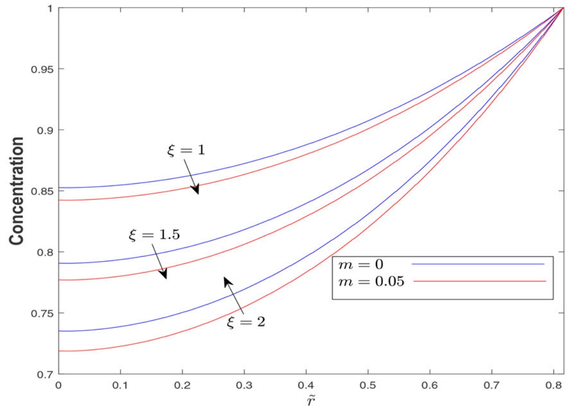

Figure 12. Concentration profile for ξ and *m*.

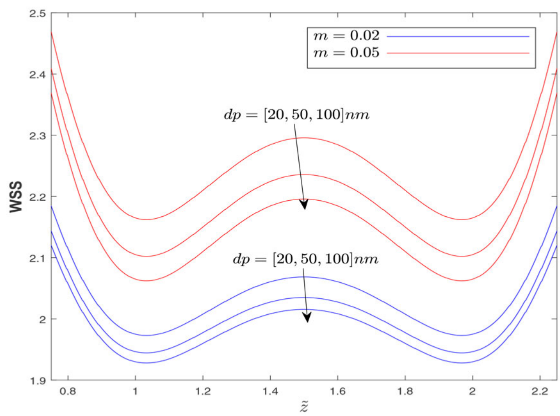

Figure 13. WSS profile for *m* and *dp*.

nanoparticle is very suitable for flow temperature. Therefore, blood flow temperature can be increased by having large sized nanoparticles in the flow. The findings of this comparative study for nanoparticle size can be adopted by clinical researchers to kill cancer cells and plaque deposition during thermal therapies by inserting large-sized nanoparticles in the artery.

Figures 11 and 12 have been developed to analyze the variation in the blood flow concentration profile for various values of the Schmidt number (*Sc*) and chemical reaction parameter (ξ) in the radial direction, respectively. In this investigation, the effect of gold nanoparticles on the fluid concentration has also been examined. The addition of nanoparticles to blood flow reduces the fluid mass diffusion process, as can be seen from Eq. (14). As a result, a decrease in the blood flow concentration profile results from an increase in the volume fraction of nanoparticles. From both, it is also concluded that the blood flow concentration profile shows a reverse trend with the increase in the values of both the Schmidt number and chemical reaction parameter. This is happening due to a reduction in molecular diffusivity with an increase in values of *Sc* and ξ; therefore, the concentration boundary layer becomes thinner.

According to the above-mentioned significance of nanoparticles in various diseases. Therefore, it is also very important to determine the nanoparticle effects on the wall shear stress (WSS) profile due to the ability of nanoparticles to move across the stenosis. Figure 13 shows the results of a numerical computation of the effect of nanoparticle volume fractions and their various sizes on

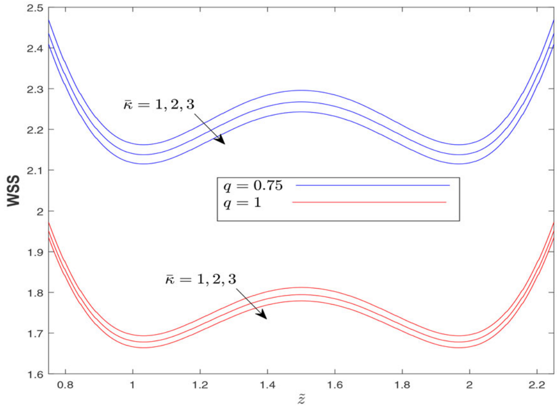

Figure 14. WSS profile for $\bar{\kappa}$ and q.

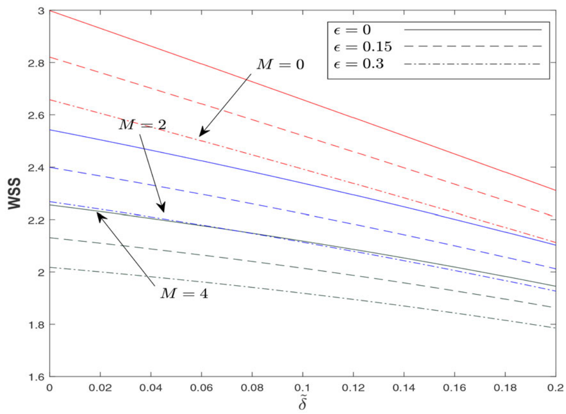

Figure 15. WSS profile for M and ε.

the WSS profile. In this investigation, the WSS profile has been computed only for the stenotic region ($\tilde{z} = .75$ to $\tilde{z} = 2.25$). This study reveals that enhancement in the volume percentage of nanoparticles in blood flow shows a significant change in the WSS profile and increases significantly with a change in the volumetric concentration of nanoparticles in the blood. This is owing due to the capability of nanoparticles to traverse across deposited plaque because, in the absence of nanoparticles, blood cells are not able to penetrate through the stenosis. Therefore, when nanoparticles are added to blood, they make a path in the deposited plaque for blood cells; therefore, the flow gets smoother at the arterial wall. This happens because, for a small-sized nanoparticle, it is a little bit easy to cross every deposited stenosis, but sometimes large-sized particles get stuck in stenosis; therefore, they can't make a sufficient path from the stenosis for the blood cells. Thus, this study suggests that the use of small-sized nanoparticles is good for achieving good results for the wall shear stress profile in a stenosed curved arterial flow.

The comparative study of a fluid's Newtonian and non-Newtonian properties on the WSS profile has been presented in Figure 14. For that, power-law fluid has been considered, and this computation examination has been performed in terms of flow behavior index (q). Here, $q < 1$ represents the fluid's shear-thinning (pseudoplastic) property, and $q = 1$ represents the fluid's Newtonian property. It is observed that as the value of flow index behavior increases, the wall shear stress profile decreases rapidly. In other words, it can be said that assuming pseudoplastic properties of blood in the mathematical modeling will be better for attaining fruitful results for the WSS profile than assuming Newtonian properties of blood. This study also analyzed the effect

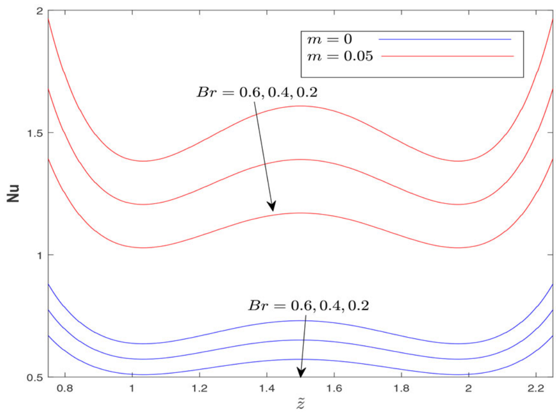

Figure 16. Nusselt number for *Br* and *m*.

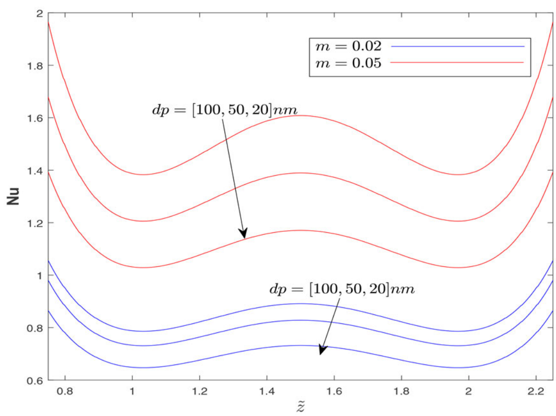

Figure 17. Nusselt number for *dp* and *m*.

of electro-kinetic width (inverse Debye length) on the WSS profile for the stenotic region. A decline in WSS profile is observed with the increase in electro-kinetic width. The obtained results for electro-kinetic width $\bar{\kappa}$ for WSS are in good agreement with the published work of Narla and Tripathi [53].

The comparative fluctuation in the WSS profile for both conditions of the magnetic field, presence ($M \neq 0$) and absence ($M = 0$), along with the curved arterial stenotic height ($\tilde{\delta}$) has been discussed in Figure 15. A linear decay in the WSS profile has been observed with the increase in stenosis height, which reveals fair agreement with the results [58,59]. This investigation has also undertaken a comparison between curved artery ($\varepsilon \neq 0$) and straight ($\varepsilon = 0$) conditions. It is concluded that with the increase in the value of arterial curvature, the blood experiences lower shear stress at the wall. Therefore, straight arteries face heavy shear stress due to higher flow velocity compared with curved arteries. The figure also describes that, with the positive improvement in magnetic field intensity, leads to increase Lorentz force power, which retards the flow speed at arterial wall. Therefore, shear stress between fluid layers decreases at arterial wall. According to the results of the curvature analysis, lipid deposition is highly likely to occur in arteries with high curvature.

The importance of the nanoparticle's presence on the heat transfer rate at the arterial wall has been computed numerically for the overlapped stenotic region using the Stones Scheme, and the results are discussed in Figure 16. From the previous results, it is well-known that with the addition of nanoparticles, the blood flow temperature increases. Therefore, in comparison with the

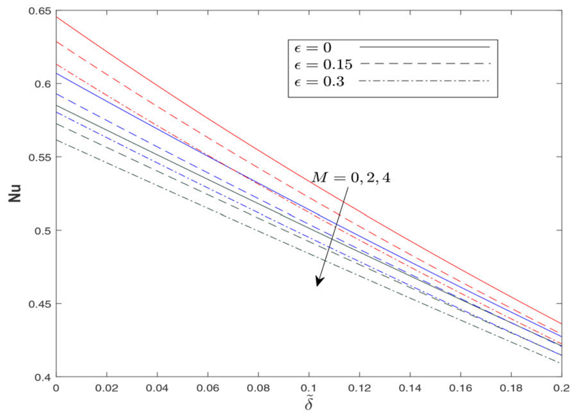

Figure 18. Nusselt number for M and ε.

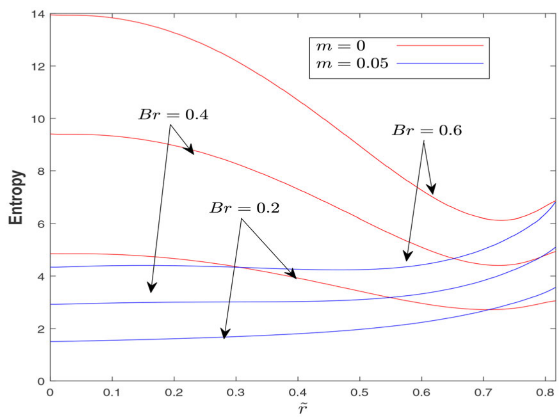

Figure 19. Entropy generation for Br and m.

absence of gold nanoparticles in blood, the heat transfer rate at the arterial wall increases significantly with the presence of nanoparticles in the flow. The impact of the Brinkmann number on the arterial heat transfer rate has also been discussed. The positive add in the Br value leads to increases in flow temperature due to a significant decay in the heat conduction rate, which was generated by viscous dissipation. Therefore, the blood heat transfer rate increases in the artery as well as its wall due to the boost in blood flow temperature with an increase in Br. Due to the significant increase in arterial wall heat transfer with the addition of nanoparticles, it will be helpful in the development of thermal therapies for clinical researchers to cure stenosis, kill cancer cells, etc. Figure 17 shows how important the size of the nanoparticles is for heat transfer at the arterial wall. This study suggests that using large-sized nanoparticles will be useful to increase arterial heat transfer in the clinical healing process. As a result, it is possible to conclude that as nanoparticle size increases, so does heat transfer at the arterial wall enhances.

Figure 18 depicts the variation in heat transfer rate for various values of arterial curvature and magnetic field intensities. This discussion has been conducted with respect to stenosis height. A linear decay in the heat transfer rate profile is observed as stenosis height increases. In other words, it can be concluded that the formation of stenosis (lipid deposition) is responsible for the decay in heat transfer rate at the arterial wall. From the figure, it can be seen that the heat transfer rate decreases by ∼33% for the artery with a 20% stenosis deposition compared with a healthy artery. A significant decline in arterial wall heat transfer rate has been observed for the increase

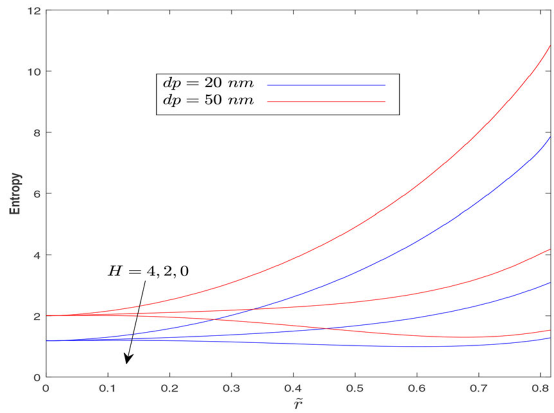

Figure 20. Entropy generation for *H* and *dp*.

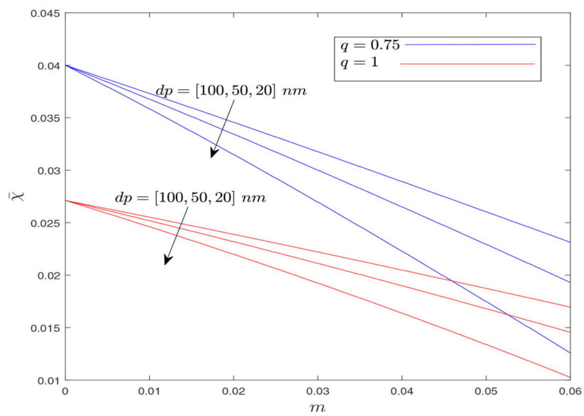

Figure 21. Energy conversion efficiency for *dp* and *q*.

in values of both arterial curvature and magnetic field intensities. This is because blood flows faster in a straight tube ($\varepsilon = 0$) than in a curved tube ($\varepsilon \neq 0$). Therefore, in curved tubes, the heat transfer rate at the arterial wall diminishes.

Entropy generation is essential to comprehending biological thermodynamics in blood flow in constricted regions of curved arteries because it represents the decrease in quality energy that can't be further utilized to do essential work. Figure 19 depicts the variation in unused energy production (entropy) in the radial direction for the different values of Brinkman number (*Br*). The preceding figures show that the blood flow temperature profile improves with an increase in the value of *Br*, resulting in greater energy in the flow. With a spike in *Br* values, a considerable increase in entropy formation is noticed due to the inability of the blood flow to convert the increased energy into useful work. This figure also provides a comparative analysis of the effects of using nanoparticles in blood flow or not using them in terms of entropy production. From the figure, it is noticed that in the absence of nanoparticles, flow generates more entropy in the center region of the artery due to the high speed of flow there, and that afterward, entropy decreases as blood reaches the wall. Entropy also increases near the arterial wall due to the presence of useful nutrients, proteins, sugars, fats, etc. It is also observed that in the presence of nanoparticles, the entropy production is lower at the center of the artery than in the rest of the arterial flow region. This happens because, with the addition of nanoparticles, the flow velocity decreases; therefore, it generates less energy in the center region of the artery due to less fluid friction. It is

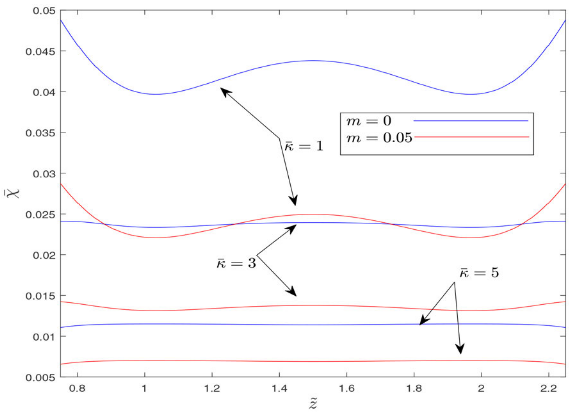

Figure 22. Energy conversion efficiency for $\bar{\kappa}$ and *m*.

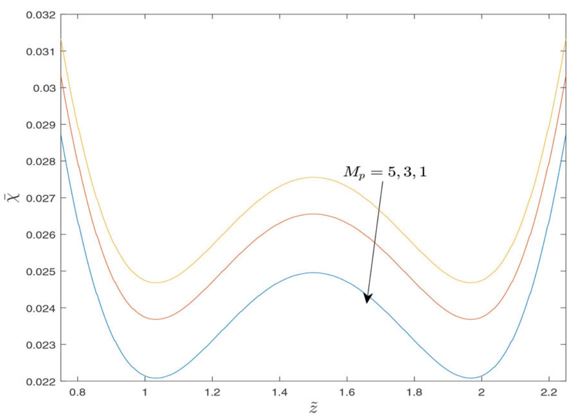

Figure 23. Energy conversion efficiency for M_p.

also notable that the flow is smooth near the stenosis in the presence of nanoparticles; therefore, at the near arterial wall, a sudden spike in entropy generation can be easily visualized.

The present comparative study is analyzing the importance of nanoparticle size on blood flow, therefore, Figure 20 illustrates the significance of gold nanoparticle size on the flow efficiency of entropy generation. This figure states that for a fixed volume fraction of nanoparticles, the entropy generation rate increases rapidly with the mixing of large-diameter nanoparticles. This is happen due to an increase in blood flow temperature for the larger-sized nanoparticle, therefore it produces more energy in blood flow. This figure also shows that the flow produced more entropy with the increase in external heating intensity.

The analysis of the conversion efficiency of blood flow mechanical energy into electro-kinetic energy with the different volume fractions of gold nanoparticles has been simulated numerically and explained in Figure 21. The figure shows that when a nanoparticle is added to the flow, it reduces the flow's conversion efficiency for converting mechanical and chemical energy into electrokinetic energy. Therefore, the increase in gold nanoparticle volume fraction reflects the sharp decline in the EKEC ($\bar{\chi}$) profile. The obtained relationship between the nanoparticle volume fraction and EKEC is in fairly good agreement with the findings of Xie and Jian [10]. This figure also reveals that adding large-sized gold nanoparticles is important for blood flow to enhance its electrokinetic energy conversion efficiency. As a result, it can be concluded that EKEC ($\bar{\chi}$) efficiency increases with an increase in nanoparticle size. It should also be noted that for a higher

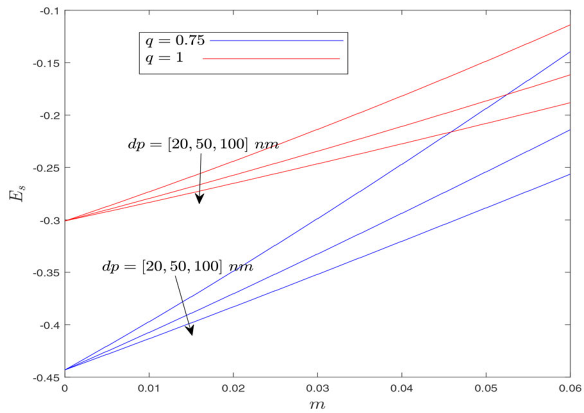

Figure 24. Streaming potential for *dp* and *q*.

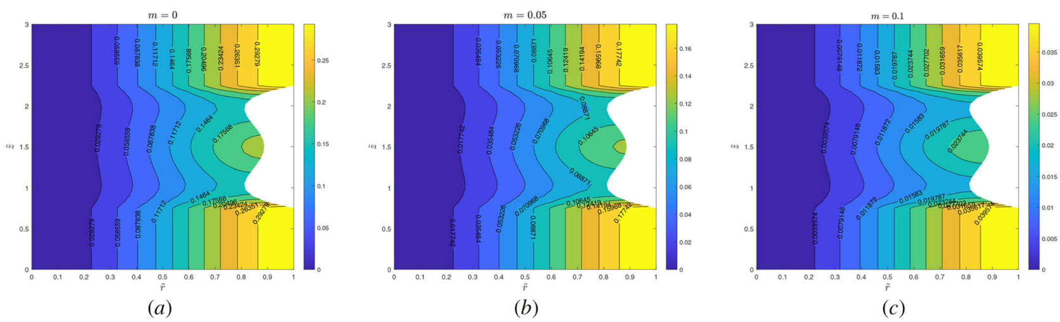

Figure 25. Stream function plot for nanoparticle volume fraction, (a) $m = 0$, (b) $m = .05$, and (c) $m = .1$.

amount of gold nanoparticles, the decay rate of the EKEC profile is faster for the small sized nanoparticles than for the larger sized nanoparticles.

The fluctuation in EKEC efficiency profile for the whole stenotic region ($0.75 \le z \le 2.25$) has been presented in Figures 22 and 23. Both figures reveal that EKEC efficiency decreases with an increase in stenosis depth at the arterial wall. Therefore, it can be concluded that the conversion rate of mechanical and chemical energy into electrokinetic energy is higher for the healthy artery than the diseased artery. Figure 22, replicates that as the value of $\bar{\kappa}$ increases i.e. decrease in EDL thickness, the EKEC efficiency decreases. This is happening because the quantity of charged ions increases with the significant distance from the arterial wall for a large EDL thickness (small $\bar{\kappa}$), which used to counter the surface-charged ions. Therefore, this hike in charged ions increases the flow EKEC efficiency for the small value of $\bar{\kappa}$. The reverse effect on the EKEC efficiency profile has been observed for conduction current (inverse ionic Peclet number). The significant increment in the $\bar{\chi}$ profile with the increases in M_p has been observed, and this variation is depicted in Figure 23.

Figure 24 illustrates the variation in the streaming potential profile as a function of gold nanoparticle volume fraction for the various values of nanoparticle size. It is well-known that gold nanoparticles have a higher electrical conductivity than blood. When added to the blood, they completely bind up the blood cells and increase their electrical conductivity. Therefore, it can be noted that with the increase in nanoparticle quantity, the electric potential of the fluidic system enhances. As a result, the streaming potential for blood flow increases as the number of nanoparticles increases. On the other hand, this study suggests that the streaming potential profile reflects the reverse effects of the increase in nanoparticle size. In other words, it can be said that the blood electric potential efficiency can be amplified by using small-sized gold nanoparticles. The

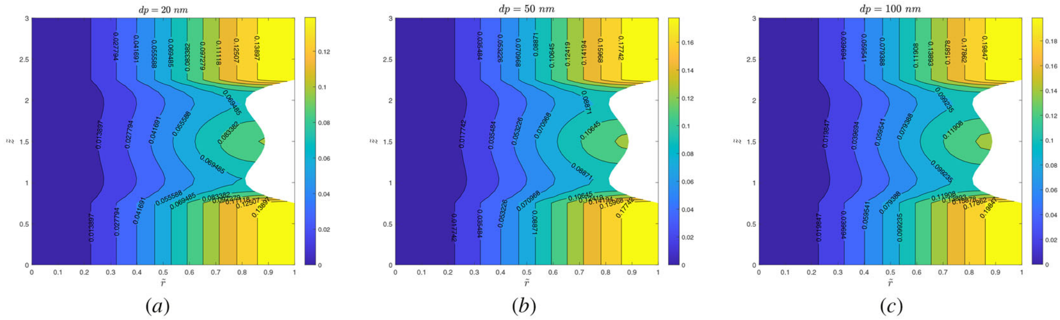

Figure 26. Stream function plot for nanoparticle size, (a) $dp = 20\,\text{nm}$, (b) $dp = 50\,\text{nm}$, and (c) $dp = 100\,\text{nm}$.

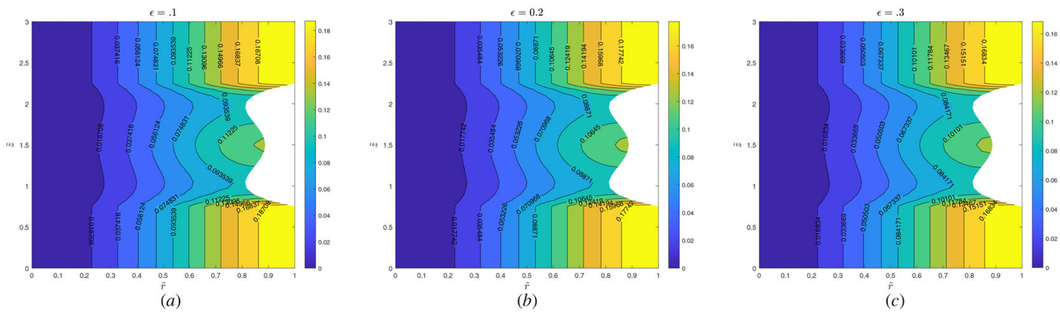

Figure 27. Stream function plot for arterial curvature, (a) $\varepsilon = 0.1,$ (b) $\varepsilon = 0.2,$ and (c) $\varepsilon = 0.3.$

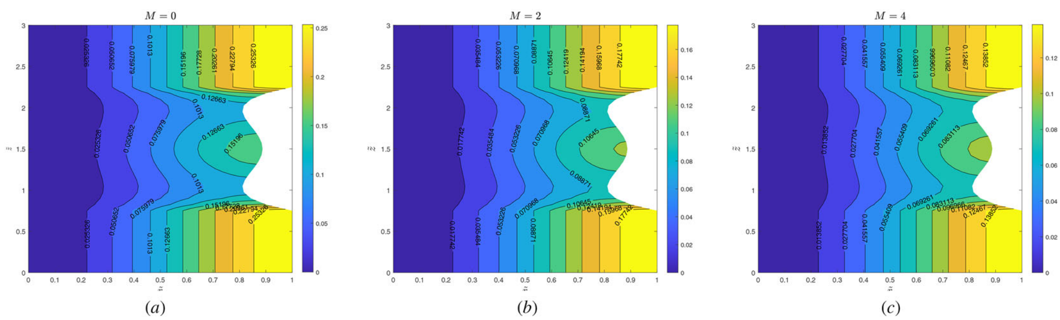

Figure 28. Stream function plot for magnetic field intensity, (a) $M = 0$, (b)$M = 2$, and (c) $M = 4$.

comparative analysis between assuming blood as pseudoplastic nature or a Newtonian nature has also been presented. It is obtained that when blood's Newtonian properties are considered, the streaming potential is higher than when considering the pseudoplastic fluid properties.

A fascinating phenomenon is to describe blood-trapping flow patterns in an overlapped stenosed curved artery by treating blood as a non-Newtonian fluid (Power-law). This phenomenon is highly important for researching blood flow mechanics in the complex arterial geometries usually associated with stenoses. Understanding these flow traps could help researchers create better treatments for cardiovascular disorders. Under certain circumstances, streamlines in the wave frame separate to catch a bolus that travels at the same pace as the wave. The complete flow

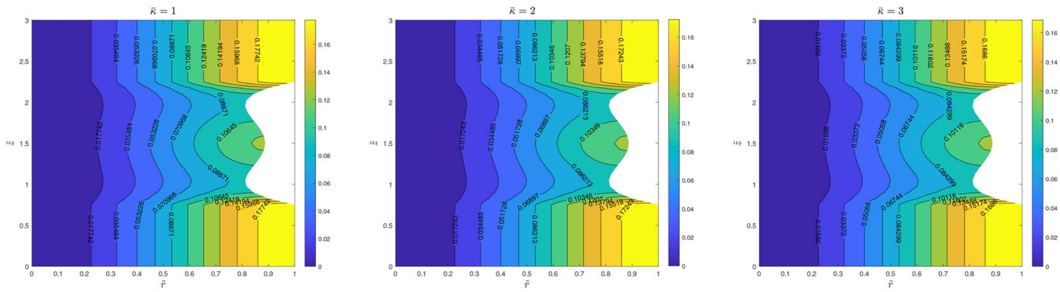

(a) (b) (c)

Figure 29. Stream function plot for inverse of Debye length, (a) $\bar{\kappa} = 1$, (b) $\bar{\kappa} = 2$, and (c) $\bar{\kappa} = 3$.

trapping pattern for blood in a curved artery for various physical parameters, such as gold nanoparticle volume fraction (m), nanoparticle diameter size (dp), arterial curvature (ε), magnetic field intensity (M), and inverse Debye length (κ) have been described using Figures 22–25. These figures also provide a comparative analysis of various values of these physical parameters. Figure 25, which provides the influence of nanoparticle presence on blood flow. From the figure, it can be seen that the size of the bolus reduces when gold nanoparticles are added to the blood flow. This is happening because gold nanoparticles are more viscous than blood; therefore, these particles form bonds with fluid cells and slow the flow speed. Figure 26 discusses the importance of nanoparticle size on the flow trapping pattern for a fixed quantity of nanoparticles in blood. The figure concluded that, when large-size nanoparticles are used for any therapy process, they smooth the flow pattern due to an increase in blood flow velocity with an increase in nanoparticle diameter. The main influence of large-sized nanoparticles is seen near the arterial wall rather than in the center area of the artery. Figures 27 and 28 illustrate the comparative effect of arterial curvature and magnetic field intensity on the flow trapping pattern. From the both figures, it is observed that the size of the bolus formation and smoothness in flow trapping decrease with the increase in values of arterial curvature and magnetic field intensity. From these, it can be concluded that, in realistic situations, most of the arteries have a high curvature; therefore, they have a higher chance for lipid/stenosis deposition due to less smoothness in blood flow. The blood flow trapping pattern for various values of inverse Debye length ($\bar{\kappa}$) has been depicted in Figure 29. This figure illustrates that to counter the surface charged ions, the quantity of charged ions increases with the increase in EDL thickness. Therefore, the flow becomes smoother with the increase in EDL thickness.

6. Conclusion

A computational examination of blood flow through an overlapped stenotic curved artery has been performed in the presence of gold nanoparticles in the blood flow. To make this investigation more plausible, a patient-specific stenosed arterial model and the non-Newtonian fluid (power-law fluid) properties of blood have been taken into account. The effect of nanoparticle size has also been analyzed. The study of electric potential (Poission–Boltzmann equation) is performed, therefore the arterial wall is considered negatively charged. The second-order central difference method has been adopted for discretized governing equations, and Stone's strongly implicit approach is used to solve these non-linear discretized equations. The effects of various physical parameters within their feasible range on the fluid velocity, temperature, concentration, EKEC, entropy, WSS, and Nusselt number have been studied using" MATLAB" software. Clinical researchers and biologists may use the results of this computational study to forecast endothelial cell damage and plaque deposition in curved arteries with WSS profiles, by which the severity of these conditions can be reduced. In treating stenosis, cancer cells, muscular discomfort, stiffness, etc., employing nanoparticles and external heating sources in blood flow would be advantageous. The following are some noteworthy findings from the current mathematical investigation:

- The blood flows velocity decreases with the addition of gold nanoparticles and reflects a reverse trend with the increase in nanoparticle size.
- The flow velocity becomes high for the thin size of the electric double layer (EDL).
- Adding gold nanoparticles and lipid deposition in blood flow reduces the efficiency of electrokinetic energy conversion (EKEC).
- The electrokinetic energy conversion (EKEC) efficiency increases more quickly with increasing EDL thickness and nanoparticle size.
- The considerable increase in blood entropy production arises whenever viscous heating is boosted, and large-sized nanoparticles are introduced into the flow.
- Arteries with high curvature have a higher possibility for lipid and stenosis deposition due to decay in the wall shear stress and heat transfer rate profile.
- The gold nanoparticles increase the blood temperature and heat transfer across arterial walls; therefore, its use can reduce lipid deposition in CVD treatments.
- The presence of gold nanoparticles reduces the blood mass diffusion process; therefore blood flow concentration profile diminishes.

ORCID

Bhupendra K. Sharma http://orcid.org/0000-0002-2051-9681
Muhammad Mubashir Bhatti http://orcid.org/0000-0002-3219-7579

References

[1] S. Das and S. Chakraborty, "Analytical solutions for velocity, temperature and concentration distribution in electroosmotic microchannel flows of a non-Newtonian bio-fluid," *Anal. Chim. Acta*, vol. 559, no. 1, pp. 15–24, 2006. DOI: 10.1016/j.aca.2005.11.046.

[2] S. Chakraborty, "Electroosmotically driven capillary transport of typical non-Newtonian biofluids in rectangular microchannels," *Anal. Chim. Acta*, vol. 605, no. 2, pp. 175–184, 2007. DOI: 10.1016/j.aca.2007.10.049.

[3] C. Zhao, E. Zholkovskij, J. H. Masliyah, and C. Yang, "Analysis of electroosmotic flow of power-law fluids in a slit microchannel," *J. Colloid Interface Sci.*, vol. 326, no. 2, pp. 503–510, 2008. DOI: 10.1016/j.jcis.2008.06.028.

[4] N. Nekoubin, "Electroosmotic flow of power-law fluids in curved rectangular microchannel with high zeta potentials," *J. Non-Newtonian Fluid Mech.*, vol. 260, pp. 54–68, 2018. DOI: 10.1016/j.jnnfm.2018.06.005.

[5] Z. Ding, K. Tian, and Y. Jian, "Electrokinetic flow and energy conversion in a curved microtube," *Appl. Math. Mech. Engl. Ed.*, vol. 43, no. 8, pp. 1289–1306, 2022. DOI: 10.1007/s10483-022-2886-5.

[6] D. Lu, S. Noreen, S. Waheed, and D. Tripathi, "Heat transfer applications in curved micro-channel driven by electroosmosis and peristaltic pumping," *J. Mech. Med. Biol.*, vol. 22, no. 5, pp. 2250030, 2022. DOI: 10.1142/S0219519422500300.

[7] S. Noreen and S. Waheed, "Study of heat characteristics of electroosmotic mediator and peristaltic mechanism via porous microtube," *BioNanoScience*, vol. 11, no. 2, pp. 476–488, 2021. DOI: 10.1007/s12668-020-00815-0.

[8] A. Bandopadhyay and S. Chakraborty, "Steric-effect induced alterations in streaming potential and energy transfer efficiency of non-Newtonian fluids in narrow confinements," *Langmuir*, vol. 27, no. 19, pp. 12243–12252, 2011. DOI: 10.1021/la202273e.

[9] S. Sarkar, "Streaming-potential-mediated pressure-driven transport of Phan–Thien–Tanner fluids in a microchannel," *Phys. Rev. E*, vol. 101, no. 5-1, pp. 053104, 2020. DOI: 10.1103/PhysRevE.101.053104.

[10] Z. Xie and Y. Jian, "Electrokinetic energy conversion of nanofluids in MHD-based microtube," *Energy*, vol. 212, pp. 118711, 2020. DOI: 10.1016/j.energy.2020.118711.

[11] N. Li, G. Zhao, X. Gao, Y. Zhang, and Y. Jian, "The impacts of viscoelastic behavior on electrokinetic energy conversion for Jeffreys fluid in microtubes," *Nanomaterials*, vol. 12, no. 19, pp. 3355, 2022. DOI: 10.3390/nano12193355.
[12] A. Z. Wilczewska, K. Niemirowicz, K. H. Markiewicz, and H. Car, "Nanoparticles as drug delivery systems," *Pharmacol. Rep.*, vol. 64, no. 5, pp. 1020–1037, 2012. DOI: 10.1016/s1734-1140(12)70901-5.
[13] S. Bamrungsap, et al., "Nanotechnology in therapeutics: a focus on nanoparticles as a drug delivery system," *Nanomedicine*, vol. 7, no. 8, pp. 1253–1271, 2012. DOI: 10.2217/nnm.12.87.
[14] R. Weissleder, G. Elizondo, J. Wittenberg, C. Rabito, H. Bengele, and L. Josephson, "Ultrasmall superparamagnetic iron oxide: characterization of a new class of contrast agents for MR imaging," *Radiology*, vol. 175, no. 2, pp. 489–493, 1990. DOI: 10.1148/radiology.175.2.2326474.
[15] R. Duivenvoorden, et al., "A statin-loaded reconstituted high-density lipoprotein nanoparticle inhibits atherosclerotic plaque inflammation," *Nat. Commun.*, vol. 5, no. 1, pp. 1–12, 2014. DOI: 10.1038/ncomms4065.
[16] J. S. Weinstein, et al., "Superparamagnetic iron oxide nanoparticles: diagnostic magnetic resonance imaging and potential therapeutic applications in neurooncology and central nervous system inflammatory pathologies, a review," *J. Cereb. Blood Flow Metab.*, vol. 30, no. 1, pp. 15–35, 2010. DOI: 10.1038/jcbfm.2009.192.
[17] A. Zaman, N. Ali, and M. Sajjad, "Effects of nanoparticles (Cu, TiO_2, Al_2O_3) on unsteady blood flow through a curved overlapping stenosed channel," *Math. Comput. Simul.*, vol. 156, pp. 279–293, 2019. DOI: 10.1016/j.matcom.2018.08.012.
[18] F. Sultan, N. A. Khan, M. Qasim, and M. I. Afridi, "Numerical simulation of the flow of Nano-Eyring-Powell fluid through a curved artery with time-variant stenosis and aneurysm," *J. Soc. Rheol. Jpn.*, vol. 47, no. 2, pp. 75–85, 2019. DOI: 10.1678/rheology.47.75.
[19] Poonam, B. K., Sharma, C. Kumawat, and K. Vafai, "Computational biomedical simulations of hybrid nanoparticles (Au-Al_2O_3/blood-mediated) transport in a stenosed and aneurysmal curved artery with heat and mass transfer: hematocrit dependent viscosity approach," *Chem. Phys. Lett.*, vol. 800, p. 139666, 2022. DOI: 10.1016/j.cplett.2022.139666.
[20] Y. Haik, V. Pai, and C.-J. Chen, "Development of magnetic device for cell separation," *J. Magn. Magn. Mater.*, vol. 194, no. 1–3, pp. 254–261, 1999. DOI: 10.1016/S0304-8853(98)00559-9.
[21] P. Voltairas, D. Fotiadis, and L. Michalis, "Hydrodynamics of magnetic drug targeting," *J. Biomech.*, vol. 35, no. 6, pp. 813–821, 2002. DOI: 10.1016/s0021-9290(02)00034-9.
[22] M. F. Barnothy, *Biological Effects of Magnetic Fields*. New York: Plenum Press, 1964.
[23] M. Freeman, A. Arrott, and J. Watson, "Magnetism in medicine," *J. Appl. Phys.*, vol. 31, no. 5, pp. S404–S405, 1960. DOI: 10.1063/1.1984765.
[24] F. Issacci, N. Ghoniem, and I. Catton, "Magnetohydrodynamic flow in a curved pipe," *Phys. Fluids*, vol. 31, no. 1, pp. 65–71, 1988. DOI: 10.1063/1.866578.
[25] Y. Kinouchi, H. Yamaguchi, and T. Tenforde, "Theoretical analysis of magnetic field interactions with aortic blood flow," *Bioelectromagnetics*, vol. 17, no. 1, pp. 21–32, 1996. DOI: 10.1002/(SICI)1521-186X(1996)17:1<21::AID-BEM3>3.0.CO;2-8.
[26] K. S. Mekheimer, M. H. Haroun, and M. El Kot, "Induced magnetic field influences on blood flow through an anisotropically tapered elastic artery with overlapping stenosis in an annulus," *Can. J. Phys.*, vol. 89, no. 2, pp. 201–212, 2011. DOI: 10.1139/P10-103.
[27] A. Farooq, M. Kahshan, S. Saleem, M. Rahimi-Gorji, and F. S. Al-Mubaddel, "Entropy production rate in ciliary induced flows through cylindrical tubules under the consequences of Hall effect," *J. Taiwan Inst. Chem. Eng.*, vol. 120, pp. 207–217, 2021. DOI: 10.1016/j.jtice.2021.03.024.
[28] B. Sharma, C. Kumawat, and O. Makinde, "Hemodynamical analysis of MHD two phase blood flow through a curved permeable artery having variable viscosity with heat and mass transfer," *Biomech. Model. Mechanobiol.*, vol. 21, pp. 797–825, 2022.
[29] S. V. Patankar and D. B. Spalding, "A calculation procedure for heat, mass and momentum transfer in three-dimensional parabolic flows," in *Numerical Prediction of Flow, Heat Transfer, Turbulence and Combustion*. Elsevier, 1983, pp. 54–73.
[30] T. Dupont, R. P. Kendall, and H. Rachford Jr., "An approximate factorization procedure for solving self-adjoint elliptic difference equations," *SIAM J. Numer. Anal.*, vol. 5, no. 3, pp. 559–573, 1968. DOI: 10.1137/0705045.
[31] A. Ahmed and S. Nadeem, "Shape effect of Cu-nanoparticles in unsteady flow through curved artery with catheterized stenosis," *Results Phys.*, vol. 7, pp. 677–689, 2017. DOI: 10.1016/j.rinp.2017.01.015.
[32] J. H. Yun, M.-S. Chun, and H. W. Jung, "The geometry effect on steady electrokinetic flows in curved rectangular microchannels," *Phys. Fluids*, vol. 22, no. 5, pp. 052004, 2010. DOI: 10.1063/1.3427572.
[33] B. K. Sharma, A. K. Jha, and R. Chaudhary, "Hall effect on MHD mixed convective flow of a viscous incompressible fluid past a vertical porous plate immersed in porous medium with heat source/sink," *Rom. J. Phys.*, vol. 52, no. 5, pp. 487–503, 2007.

[34] M. Corcione, "Empirical correlating equations for predicting the effective thermal conductivity and dynamic viscosity of nanofluids," *Energy Conv. Manag.*, vol. 52, no. 1, pp. 789–793, 2011. DOI: 10.1016/j.enconman.2010.06.072.
[35] X. Feng and D. W. Johnson, "Mass transfer in SiO_2 nanofluids: a case against purported nanoparticle convection effects," *Int. J. Heat Mass Transf.*, vol. 55, no. 13–14, pp. 3447–3453, 2012. DOI: 10.1016/j.ijheatmasstransfer.2012.03.009.
[36] U. Khanduri and B. K. Sharma, "Hall and ion slip effects on hybrid nanoparticles (Au-Go/blood) flow through a catheterized stenosed artery with thrombosis," Proceedings of the Institution of Mechanical Engineers, Part C: Journal of Mechanical Engineering Science, 2022, p. 09544062221136710. DOI: 10.1177/09544062221136710.
[37] S. Agrawal, G. Jayaraman, V. Srivastava, and K. Nigam, "Power law fluids in a circular curved tube. Part I. Laminar flow," *Polym. Plast. Technol. Eng.*, vol. 32, no. 6, pp. 595–614, 1993. DOI: 10.1080/03602559308021024.
[38] M. Ayub, I. Shahzadi, and S. Nadeem, "A Ballon model analysis with Cu-blood medicated nanoparticles as drug agent through overlapped curved stenotic artery having compliant walls," *Microsyst. Technol.*, vol. 25, no. 8, pp. 2949–2962, 2019. DOI: 10.1007/s00542-018-4263-x.
[39] P. A. Bakalis and P. M. Hatzikonstantinou, "Effect of curvature and magnetic field on MHD flow of a liquid metal in a curved annular duct," *Int. J. Numer. Methods Heat Fluid Flow*, vol. 25, no. 8, pp. 1818–1833, 2015. DOI: 10.1108/HFF-12-2013-0363.
[40] C. Kumawat, B. Sharma, Q. M. Al-Mdallal, and M. Rahimi-Gorji, "Entropy generation for MHD two phase blood flow through a curved permeable artery having variable viscosity with heat and mass transfer," *Int. Commun. Heat Mass Transf.*, vol. 133, pp. 105954, 2022. DOI: 10.1016/j.icheatmasstransfer.2022.105954.
[41] D. Young, "Effect of a time-dependent stenosis on flow through a tube," 1968.
[42] P. Goswami and S. Chakraborty, "Energy transfer through streaming effects in time-periodic pressure-driven nanochannel flows with interfacial slip," *Langmuir*, vol. 26, no. 1, pp. 581–590, 2010. DOI: 10.1021/la901209a.
[43] R. Ponalagusamy and R. Tamil Selvi, "Influence of magnetic field and heat transfer on two-phase fluid model for oscillatory blood flow in an arterial stenosis," *Meccanica*, vol. 50, no. 4, pp. 927–943, 2015. DOI: 10.1007/s11012-014-9990-1.
[44] B. Tripathi, B. K. Sharma, and M. Sharma, "Modeling and analysis of MHD two-phase blood flow through a stenosed artery having temperature-dependent viscosity," *Eur. Phys. J. Plus*, vol. 134, no. 9, pp. 466, 2019. DOI: 10.1140/epjp/i2019-12813-9.
[45] A. Bejan, "Study of entropy generation in fundamental convective heat transfer," 1979.
[46] N. A. Khan, F. Naz, and F. Sultan, "Entropy generation analysis and effects of slip conditions on micropolar fluid flow due to a rotating disk," *Open Eng.*, vol. 7, no. 1, pp. 185–198, 2017. DOI: 10.1515/eng-2017-0025.
[47] N. A. Khan, S. Aziz, and S. Ullah, "Entropy generation on MHD flow of Powell-Eyring fluid between radially stretching rotating disk with diffusion-thermo and thermo-diffusion effects," *Acta Mech. Autom.*, vol. 11, no. 1, pp. 20–32, 2017. DOI: 10.1515/ama-2017-0004.
[48] I. Shahzadi and S. Ijaz, "On model of hybrid Casson nanomaterial considering endoscopy in a curved annulas: a comparative study," *Phys. Scr.*, vol. 94, no. 12, pp. 125215, 2019. DOI: 10.1088/1402-4896/ab34bb.
[49] B. K. Sharma and C. Kumawat, "Impact of temperature dependent viscosity and thermal conductivity on MHD blood flow through a stretching surface with ohmic effect and chemical reaction," *Nonlinear Eng.*, vol. 10, no. 1, pp. 255–271, 2021. DOI: 10.1515/nleng-2021-0020.
[50] B. Tripathi and B. Sharma, "Effect of variable viscosity on MHD inclined arterial blood flow with chemical reaction," *Int. J. Appl. Mech. Eng.*, vol. 23, no. 3, pp. 767–785, 2018. DOI: 10.2478/ijame-2018-0042.
[51] Y. Gan, *Continuum Mechanics - Progress in Fundamentals and Engineering Applications*. London: IntechOpen, 2012.
[52] K. S. Mekheimer, A. Zaher, and W. Hasona, "Entropy of AC electro-kinetics for blood mediated gold or copper nanoparticles as a drug agent for thermotherapy of oncology," *Chinese J. Phys.*, vol. 65, pp. 123–138, 2020. DOI: 10.1016/j.cjph.2020.02.020.
[53] V. Narla and D. Tripathi, "Electroosmosis modulated transient blood flow in curved microvessels: study of a mathematical model," *Microvasc. Res.*, vol. 123, pp. 25–34, 2019. DOI: 10.1016/j.mvr.2018.11.012.
[54] V. Narla, D. Tripathi, and O. A. Bég, "Electro-osmotic nanofluid flow in a curved microchannel," *Chinese J. Phys.*, vol. 67, pp. 544–558, 2020. DOI: 10.1016/j.cjph.2020.08.010.
[55] N. K. Mishra, M. Sharma, B. Sharma, and U. Khanduri, "Soret and Dufour effects on MHD nanofluid flow of blood through a stenosed artery with variable viscosity," *Int. J. Mod. Phys. B*, p. 2350266, 2023. DOI: 10.1142/S0217979223502661.

[56] R. Gandhi, B. Sharma, C. Kumawat, and O. A. Bég, “Modeling and analysis of magnetic hybrid nanoparticle (Au-Al_2O_3/blood) based drug delivery through a bell-shaped occluded artery with joule heating, viscous dissipation and variable viscosity effects,” Proceedings of the Institution of Mechanical Engineers, Part E: Journal of Process Mechanical Engineering, 2022, p. 09544089221080273. DOI: 10.1177/09544089221080273.

[57] B. Sharma, R. Gandhi, and M. Bhatti, “Entropy analysis of thermally radiating MHD slip flow of hybrid nanoparticles (Au-Al_2O_3/Blood) through a tapered multi-stenosed artery,” *Chem. Phys. Lett.*, vol. 790, pp. 139348, 2022. DOI: 10.1016/j.cplett.2022.139348.

[58] C. Kumawat, B. Sharma, and K. Mekheimer, “Mathematical analysis of two-phase blood flow through a stenosed curved artery with hematocrit and temperature dependent viscosity,” *Phys. Scr.*, vol. 96, no. 12, pp. 125277, 2021. DOI: 10.1088/1402-4896/ac454a.

[59] K. S. Mekheimer and M. El Kot, “Suspension model for blood flow through catheterized curved artery with time-variant overlapping stenosis,” *Eng. Sci. Technol.*, vol. 18, no. 3, pp. 452–462, 2015. DOI: 10.1016/j.jestch.2015.03.010.